ATM Deficiency Induces TGFβ-Mediated Stromal Programming in Pancreatic Cancer

Elodie Roger[1], Hannah M. Mummey[2], Eleni Zimmer[1], Dharini Srinivasan[1], Anna Härle[1], Loïc Moubri[3], Alica K. Michels[4,5], Rima Singh[5], Menar Ekizce[1], Michael K. Melzer[1,6], Yun Lee[7], Austin Silva[5], Luisa Härle[1], Thomas Engleitner[8,9], Frank Arnold[1], Mareen Morawe[4], Benjamin Karem Naggay[10], Juliane Schneider[11], Leonard Gilberg[12], Julia P. Mosler[1], Christina Ludwig[13], Chen Meng[13], Maximilian Hirschenberger[14], Victoria Hunszinger[14], Klaus Kluck[15], Martina Kirchner[15], Anna-Lena Volckmar[15,16,17], Mareike Wirth[18], Mohamed S.S. Alhamdani[19], Jörg D. Hoheisel[19], J.-Matthias Löhr[20], Thomas Seufferlein[4], Alireza Abaei[18], Ralf Kemkemer[10,21], Roland Rad[8,9,12,22], Jan Budczies[15,16,17], Medhanie A. Mulaw[23], Patrick C. Hermann[4], Mark M. Haenle[4], Konstantin M.J. Sparrer[14,24], Christopher J. Halbrook[5], Kyle J. Gaulton[7], Konrad Steinestel[11], Albrecht Stenzinger[15,16,17], Nelson Dusetti[3], Lukas Perkhofer[1,25], Johann Gout[1], and Alexander Kleger[1,25,26]

ABSTRACT

The tumor microenvironment (TME) actively contributes to pancreatic ductal adenocarcinoma (PDAC) pathogenesis through dynamic bidirectional tumor–stroma interactions. In this study, we demonstrated that ATM-deficient tumor epithelium reprograms the TME in a genotype-specific manner to enhance cancer aggressiveness. In genetically engineered mouse models, pancreatic stellate cell and cancer-associated fibroblast (CAF) coculture systems, single-nucleus multiomics, and human PDAC models, tumoral loss of ATM serine/threonine kinase drove CAFs toward αSMA$^+$ myofibroblastic (myCAF) differentiation, independently of p53 status. The myCAFs, in turn, promoted cancer aggressiveness and chemoresistance. Mechanistically, ATM deficiency increased reactive oxygen species and contractility signaling, enhancing TGFβ1 secretion. Pharmacologic TGFβ inhibition reversed myCAF differentiation, sensitized tumors to chemotherapy, and impaired tumor progression in both murine and human ATM-null models. These findings reveal that ATM-deficient tumors shape a cancer-promoting niche via TGFβ signaling and identify dual targeting of intrinsic and extrinsic vulnerabilities as a promising precision oncology strategy.

Significance: TGF-β-driven myofibroblastic stromal differentiation in ATM-deficient pancreatic cancer generates a genotype-specific tumor microenvironment, providing a targetable axis and highlighting the need to integrate epithelial genotype and stromal context in pancreatic cancer therapy.

[1]Institute of Molecular Oncology and Stem Cell Biology, Ulm University Hospital, Ulm, Germany. [2]Bioinformatics and Systems Biology Graduate Program, University of California, San Diego, La Jolla, California. [3]Cancer Research Center of Marseille (CRCM), INSERM U1068, CNRS UMR 7258, Aix-Marseille University and Paoli-Calmettes Institute, Marseille, France. [4]Department of Internal Medicine I, Ulm University Hospital, Ulm, Germany. [5]Department of Molecular Biology and Biochemistry, University of California, Irvine, California. [6]Department of Urology, Ulm University Hospital, Ulm, Germany. [7]Department of Pediatrics, University of California, San Diego, La Jolla, California. [8]Institute of Molecular Oncology and Functional Genomics, TUM School of Medicine, Technische Universität München, Munich, Germany. [9]Center for Translational Cancer Research (TranslaTUM), TUM School of Medicine, Technische Universität München, Munich, Germany. [10]School of Life Sciences, Reutlingen University, Reutlingen, Germany. [11]Institute of Pathology and Molecular Pathology, Bundeswehrkrankenhaus Ulm, Ulm, Germany. [12]Department of Medicine II, Klinikum rechts der Isar, TUM School of Medicine, Technische Universität München, Munich, Germany. [13]Bavarian Center for Biomolecular Mass Spectrometry (BayBioMS), School of Life Sciences, Technical University of Munich, Freising, Germany. [14]Institute of Molecular Virology, Ulm University Medical Center, Ulm, Germany. [15]Institute of Pathology, Heidelberg University Hospital, Heidelberg, Germany. [16]Center for Personalized Medicine (ZPM) Heidelberg, Heidelberg, Germany. [17]German Cancer Consortium (DKTK), Heidelberg partner site, Heidelberg, Germany. [18]Center for Translational Imaging (MoMAN), Ulm University, Ulm, Germany. [19]Division of Functional Genome Analysis, German Cancer Research Center (DKFZ), Heidelberg, Germany. [20]Department of Clinical Science, Intervention and Technology (CLINTEC), Pancreas Cancer Research Lab, Karolinska Institute, Stockholm, Sweden. [21]Department of Cellular Biophysics, Max Planck Institute for Medical Research, Heidelberg, Germany. [22]German Cancer Consortium (DKTK), German Cancer Research Center (DKFZ), Heidelberg, Germany. [23]Unit for Single-Cell Genomics, Medical Faculty, Ulm University, Ulm, Germany. [24]German Center for Neurodegenerative Diseases (DZNE), Ulm, Germany. [25]Division of Interdisciplinary Pancreatology, Department of Internal Medicine I, Ulm University Hospital, Ulm, Germany. [26]Core Facility Organoids, Ulm University, Ulm, Germany.

H.M. Mummey and E. Zimmer contributed equally to this article.

J. Gout and A. Kleger jointly supervised this article and contributed equally to this article.

Corresponding Authors: Alexander Kleger, Institute of Molecular Oncology and Stem Cell Biology (IMOS), Ulm University Hospital, Albert-Einstein-Allee 23, Ulm 89081, Germany. E-mail: alexander.kleger@uni-ulm.de; and Johann Gout, johann.gout@uni-ulm.de

Cancer Res 2026;XX:XX–XX

doi: 10.1158/0008-5472.CAN-26-0138

This open access article is distributed under the Creative Commons Attribution-NonCommercial-NoDerivatives 4.0 International (CC BY-NC-ND 4.0) license.

©2026 The Authors; Published by the American Association for Cancer Research

Downloaded from http://aacrjournals.org/cancerres/article-pdf/doi/10.1158/0008-5472.CAN-26-0138/3803456/can-26-0138.pdf by DKFZ - German Cancer Research Center user on 25 June 2026

Introduction

Pancreatic ductal adenocarcinoma (PDAC) remains one of the deadliest solid malignancies, with a 5-year overall survival of 13% across all stages (1). In advanced disease, treatment selection is largely based on patient performance status rather than molecular tumor characteristics (2). An exception is the PARP inhibitor olaparib, which exploits synthetic lethality with germline *BRCA1/2* mutations and other DNA damage response (DDR) gene alterations (3–8). Otherwise, targeted therapies have mostly failed, reflecting PDAC's complex biology (9). Poor outcomes are attributed to the marked heterogeneity of both the neoplastic epithelium and its tumor microenvironment (TME; ref. 10).

The TME comprises cancer-associated fibroblasts (CAF), immune, endothelial, and neuronal cells, and extracellular matrix (ECM). The components, their heterogeneity, and spatial organization shape PDAC behavior and plasticity (11). CAFs, the predominant TME cell type, exhibit diverse phenotypes and functions, forming distinct coexisting subpopulations (12). αSMA^+ myofibroblastic CAFs (myCAF) reside near tumor cells and mediate ECM production and fibrosis, whereas distant inflammatory CAFs (iCAF) display a cytokine-secreting phenotype (13). Antigen-presenting CAFs (apCAF) express MHC class II molecules and contribute to immunosuppression by inducing regulatory T cells (Treg; refs. 14, 15). The roles of these subtypes in tumor progression and therapy response remain incompletely defined and context-dependent. myCAFs can restrain progression by limiting dissemination and angiogenesis (16, 17), yet dense ECM impairs drug delivery (18). myCAF-derived factors also support proliferation and invasion (19). Consequently, nonselective stroma-targeting approaches have failed or worsened outcomes (16, 18, 20). *In vivo*, JAK/STAT inhibition, a driver of the iCAF phenotype, induced myCAF enrichment and reduced tumor growth (21), highlighting the need for selective targeting of stromal subtypes.

Although desmoplasia is a hallmark of PDAC, how tumor genotype shapes stromal programming remains poorly understood and is not exploited therapeutically. Deciphering mutation-specific epithelium–stroma molecular communications may enable personalized strategies targeting tumor-promoting cross-talk. A genomically unstable PDAC subtype with a high mutational burden frequently harbors DDR alterations and shows sensitivity to platinum-based chemotherapy (3, 22). Pathogenic DDR mutations occur in 17% to 25% of patients, most commonly affecting *ATM*, *BRCA1/2*, or *PALB2* (8, 23). This subgroup represents a clinically relevant population that may benefit from approaches targeting both epithelial vulnerabilities and genotype-specific stromal features.

ATM encodes a serine/threonine kinase essential for homologous recombination (HR) repair and is the most frequently mutated DDR gene in PDAC (5). Its loss generates HR deficiency (HRD), genomic instability, and aggressive, fibrotic, and metastatic phenotypes, while conferring sensitivity to platinum derivatives and PARP, ATR, and DNA-PK inhibitors (6–8, 24). Here, we show that epithelial ATM loss of function drives TGFβ-mediated tumor–stroma cross-talk that reprograms the surrounding niche toward a protumorigenic state, constituting an additional therapeutic vulnerability in ATM-deficient PDAC. Thus, epithelial genotype not only defines tumor-intrinsic features but also underlies TME heterogeneity and should be integrated into personalized therapeutic strategy design.

Materials and Methods

Ethics statement

All animal care and procedures followed German, US, or French legal regulations and were previously and respectively approved by the governmental review board of the state of Baden-Württemberg (Permission nos. 1273 and 1568), by the Institutional Animal Care and Use Committee of the University of California, Irvine (protocol #AUP-23-084), and by the Ethics Committee for Animal Experimentation of Marseille no.14 (approval number APAFIS 202308111552762). All aspects of mouse work were carried out following strict guidelines to ensure careful, consistent, and ethical handling of mice.

Human biomaterial was obtained from the biobank of the University Hospital of Ulm and the Universitätsklinikum Heidelberg. Written informed consent was obtained from all patients. Experiments involving human samples were conducted in accordance with the Declaration of Helsinki and were approved by the Ethics Committee of the University of Ulm (PDAC Liver Metastasis): 72/2019 (human tissue and blood) and by the Ethics Committee of the Universitätsklinikum Heidelberg (Permission no. S-315/2020).

Mice

$Atm^{fl/fl}$ (RRID: IMSR_JAX:021444), $Trp53^{fl/fl}$, $LSL\text{-}Kras^{G12D/+}$ (RRID: IMSR_JAX:008179), and $Ptf1a^{Cre/+}$ (RRID: MGI:3695166) were previously described (25–28). Male C57BL/6J mice were purchased from Janvier Labs (RRID: IMSR_RJ:C57BL-6JRJ). Female Nude-$Foxn1^{nu}$ mice were purchased from Inotiv (RRID: IMSR_ENV:HSD-069). Mice were housed and bred in a conventional health status–controlled animal facility. All aspects of the mouse work were carried out following strict guidelines to ensure careful, consistent, and ethical handling of mice.

Cell culture

$LSL\text{-}Kras^{G12D/+}$; $Ptf1a^{Cre/+}$ (KC), $Atm^{fl/fl}$; $LSL\text{-}Kras^{G12D/+}$; $Ptf1a^{Cre/+}$ (AKC), $Trp53^{fl/fl}$; $LSL\text{-}Kras^{G12D/+}$; $Ptf1a^{Cre/+}$ (KPC), and $Atm^{fl/fl}$; $Trp53^{fl/fl}$; $LSL\text{-}Kras^{G12D/+}$; $Ptf1a^{Cre/+}$ (AKPC) cell lines were derived from the corresponding mouse models and immortalized as described previously (6). Cells were cultured in DMEM containing 10% FBS and 100 IU/mL penicillin and 100 μg/mL streptomycin sulfate (P/S). MIA PaCa-2 (ATCC, CRL-1420, RRID: CVCL_0428) cells were purchased from the ATCC and were cultured in DMEM containing 10% FBS and P/S. The CRISPR-edited ATM-deficient MIA PaCa-2 cell lines were generated as previously described (8). Human pancreatic stellate cells (PSC; ref. 29) were kindly provided by Prof. J.-Matthias Löhr (Karolinska Institute) and were cultured in DMEM containing 10% FBS and P/S. CAF lines were kindly provided by Prof. Dr. Dieter Saur (Technical University of Munich) and were cultured in DMEM containing 10% FBS and P/S. Briefly, CAF lines were derived from primary PDAC cultures established from autochthonous pancreatic tumors ($Kras^{G12D/+}$; $Trp53^{+/lox}$; $Tgfbr2^{lox/lox}$ and $Kras^{G12D/+}$; $Tgfbr2^{lox/lox}$) according to protocols adapted from (13). PCR was performed to assess the absence of the recombined *Kras* band and to select CAF lines. HEK293T cells (RRID: CVCL_0063) were kindly provided by Prof. Dr. Franz Oswald (Ulm University Hospital) and were cultured in DMEM containing 10% FBS and P/S. Patient-derived organoid (PDO) lines were propagated as previously described (30).

All cells were propagated at 37°C under a 5% (v/v) CO_2 atmosphere. All experiments were performed between passages 5 and 25. The cell lines used in this study were not authenticated by short tandem repeat profiling. All cell lines were routinely tested and

Downloaded from http://aacrjournals.org/cancerres/article-pdf/doi/10.1158/0008-5472.CAN-26-0138/3803456/can-26-0138.pdf by DKFZ - German Cancer Research Center user on 25 June 2026

confirmed to be free of *Mycoplasma* contamination using the MycoSPX PCR kit (Biontex Laboratories). All experiments were conducted with at least two different cell lines per genotype.

5-Fluorouracil, AZD0156, galunisertib, irinotecan, leucovorin (folinic acid), and oxaliplatin were purchased from Selleck Chemicals. SB431542 was purchased from Axon. MRTX1133 was purchased from Biorbyt. Human IL1α was purchased from Bio-Techne. Human TGFβ1 was purchased from PeproTech. YCG063 and menadione were purchased from Merck Millipore.

Tumor cell–conditioned media were generated from 1.7×10^6 cells propagated in serum-free DMEM containing P/S for 24 hours in 10 cm dishes. Supernatants were harvested, centrifuged for cell debris elimination, and stored at −80°C. To assess CAF differentiation, PSCs were grown on Matrigel GFR-coated wells (1:4 dilution) in serum-free DMEM containing P/S. For coculture experiments, tumor cells and PSCs were seeded at a 1:1 ratio (50,000 cells each), with tumor cells in six-well translucent polystyrene inserts (0.4 μm pore size, ThinCert, Greiner Bio-One) and PSCs in the lower chamber, and propagated in serum-free DMEM containing P/S. All analyses of PSC differentiation into CAFs were conducted using the vehicle-inactivated PSC condition as a reference for normalization.

CRISPR/Cas9 editing

Parental AKC and AKPC tumor cells were nucleofected with a complex consisting of HiFi Cas9 Nuclease V3 (80 pmol, Integrated DNA Technologies) and single-guide RNA (sgRNA; 300 pmol, Integrated DNA Technologies), using gene-specific or nontargeting control sgRNAs (Integrated DNA Technologies; Supplementary Table S1). Nucleofection was carried out on a Lonza 4D-Nucleofector system using the P2 Primary Cell 4D-Nucleofector X kit (Lonza Bioscience, V4XP-2032) and pulse code DN100. Target gene knockout (KO) was confirmed by immunoblot or Sanger sequencing (Eurofins Genomics).

Colony formation assay

Tumor cells were seeded in 24-well plates and cocultured with PSCs seeded (1:2 ratio; respectively, 12,000 tumor cells and 24,000 PSCs) in Matrigel-coated polycarbonate cell culture inserts (3 μm pore size, Nunc) in serum-free DMEM containing P/S for 24 hours prior to treatment. Cocultures were then treated for 48 hours with 6 μmol/L oxaliplatin. Tumor cells were fixed with cold 4% formaldehyde and stained with 4% Giemsa. Images were captured using an iPhone 11 (Apple). Acquired pictures were subsequently analyzed using ImageJ software (RRID: SCR_003070).

Cell viability assay

Tumor cells were seeded in 96-well plates (1,000–5,000 cells/well). After attachment, cells were treated for 72 hours. Viability was measured using an MTT assay (Sigma-Aldrich) according to the manufacturer's instructions. Absorbance was measured at a wavelength of 590 nm using a Tecan Infinite M200 Pro Multimode Microplate Reader (RRID: SCR_019033). Viability percentages were normalized to vehicle-treated cell viability.

TGFβ reporter assay

HEK293T cells (RRID: CVCL_0063), used as recipient cells for the TGFβ reporter assay, were kindly provided by Prof. Dr. Franz Oswald (Ulm University Hospital). HEK293T cells were transfected with the pGL3-(CAGA)12-MLP-Luc (31) and Renilla (phRL-CMV) plasmids prior to treatment with tumor cell–conditioned media. Briefly, HEK293T cells were transfected using 2 μL of Lipofectamine 2000 reagent (Invitrogen) in Opti-MEM medium. After 6 h, the medium was replaced with conditioned media from tumor cells or serum-free DMEM containing P/S. After 48 hours, the Dual-Luciferase Reporter Assay (Promega) was used following the manufacturer's recommendations, and the luminescence values were determined for each condition with a Tecan Infinite M200 Pro Multimode Microplate Reader (RRID: SCR_019033). Renilla luminescence values were used for correction to determine Luciferase luminescence corrected values. Luciferase luminescence corrected values were normalized to untreated transfected HEK293T cells, which were used as a reference for basal reporter activity.

TGFβ1 ELISA

Tumor cells were propagated for 24 hours in serum-free DMEM containing P/S. Supernatants were collected and processed following the manufacturer's instructions (Quantikine Human/Mouse/Rat/Porcine/Canine TGFβ1 Immunoassay, R&D Systems).

Reactive oxygen species level quantification

Ten thousand tumor cells were seeded in a black 96-well plate in DMEM containing 10% FBS and P/S. After attachment, the culture medium was replaced with serum-free DMEM containing P/S for 24 hours and processed following the manufacturer's recommendations for ROS level quantification (ROS-Glo H2O2 Assay, Promega). Luminescence was measured with a Tecan Infinite M200 Pro Multimode Microplate Reader (RRID: SCR_019033).

Microchannel single-cell migration assay

The microchannel chips were processed as previously described (32). Collagen I–coated chips and 11 μm wide microchannels were used to assess single-cell migration. Ten thousand tumor cells were added to the invasion chip and cultured in a 0% to 10% FBS gradient. Phase contrast live-cell imaging was performed in a temperature-controlled culture chamber equipped with a ZEISS Axiovert 200M inverted microscope. Images were captured every 10 minutes for 24 hours. Acquired pictures were subsequently analyzed using ImageJ software (RRID: SCR_003070). Permeative cells were defined as tumor cells that left the 0% FBS chamber, entered the channels, and exited the opposite 10% FBS side.

Wound healing assay

Assays using the AKC tumor cell lines treated or not with ROS inhibitor were conducted as follows: 300,000 tumor cells were seeded in 48-well plates in DMEM containing 10% FBS and P/S. After attachment, cell monolayers were scratched using sterile tips, and the medium was replaced with serum-free DMEM containing P/S for 48 hours. Brightfield images were acquired after 0, 24, and 48 hours and analyzed using ImageJ software (RRID: SCR_003070).

Assays using CRISPR-edited AKC and AKPC tumor cell lines were conducted using a Sartorius Incucyte SX5 Live Cell Analysis System (RRID: SCR_026298) as follows: 50,000 cells/well were seeded in Sartorius Incucyte ImageLock 96-well microplates in DMEM containing 10% FBS and P/S. After attachment, uniform scratch wounds were generated using the Incucyte 96-well WoundMaker tool, and the medium was replaced with serum-free DMEM containing P/S. Wound closure was monitored for 24 hours. The percentages of wound closure were calculated with the following equation: (Tx wound area/T0 wound area) * 100.

Downloaded from http://aacrjournals.org/cancerres/article-pdf/doi/10.1158/0008-5472.CAN-26-0138/3803456/can-26-0138.pdf by DKFZ - German Cancer Research Center user on 25 June 2026

Ex vivo coculture assay on porcine urinary bladder

Porcine urinary bladders (PUB) were processed as described previously (33). Briefly, PUBs were deepithelialized and sterilized with 0.1% peroxyacetic acid and maintained at an air–liquid interface in 6-well plates containing DMEM/F-12 supplemented with 2% P/S. Tumor cells and PSCs (1:3 ratio; respectively, 166,000 tumor cells and 500,000 PSCs) were seeded onto the PUB surface inside 5-mm plastic rings in a 1:1 serum-free DMEM/F-12:Matrigel GFR solution. After 5 days, cocultures were treated for 3 days with FOLFIRINOX (75 nmol/L 5-fluorouracil, 25 nmol/L irinotecan, and 5 nmol/L oxaliplatin) and/or 10 μmol/L of the TGFBR1 inhibitor SB431542. PUBs were then fixed and processed for histology as previously described (33).

Immunostaining

For immunocytofluorescence, cells grown on glass coverslips were fixed in cold 4% formaldehyde and permeabilized with 0.05% Tween 20 for 20 minutes. Matrigel GFR coating of glass coverslips was performed prior to PSC seeding. F-Actin was stained with phalloidin-Atto565 (1:500–1:1,000; Sigma-Aldrich). All histologic experiments were performed as previously described (6, 24) or according to standard protocols on formalin-fixed, paraffin-embedded tissues.

For immunofluorescence, primary antibodies against ACTN4 (1:250; Abcam, ab108198, RRID: AB_10858236), αSMA (1:500–1:1,000; Abcam, ab7817, RRID: AB_262054), B220 (1:25; Santa Cruz Biotechnology, sc-19597, RRID: AB_627078), CD11b (1:100; Cell Signaling Technology, 46512, RRID: AB_3095061), CDH1 (1:250; Cell Signaling Technology, 3195, RRID: AB_2291471), CDH2 (1:200; Cell Signaling Technology, 13116, RRID: AB_2687616), CK19 (1:35; Developmental Studies Hybridoma Bank, 2133570, RRID: AB_2133570), CTGF (1:50; Santa Cruz Biotechnology, sc-365970, RRID: AB_10917259), CXCL2 (1:50; clone EPR28746-89; Abcam, ab317569), H2AX p-S139 (1:1,000; Cell Signaling Technology, 9718, RRID: AB_2118009), Ly6C (1:200; clone RM1151; Abcam, ab317272), P53 (1:2,000; Cell Signaling Technology, 2524, RRID: AB_331743), PDPN (1:200; BioLegend, 127404, RRID: AB_1134222), POSTN and CD11b (1:100; clone E4K8C; Cell Signaling Technology, 93169), PXN (1:100; clone 5H11; Invitrogen, AHO0492), SMAD2 p-S465/467 (1:100–1:200; Cell Signaling Technology, 3108, RRID: AB_490941), STAT3 p-Y705 (1:200; Cell Signaling Technology, 9145, RRID: AB_2491009), TJP1 (1:250; clone 1A12; Invitrogen, 33-9100), and VINC (1:250; clone 42H89L44; Invitrogen, 700062) were used.

The secondary antibodies were anti-rabbit Alexa Fluor 647 dye-conjugated (Invitrogen A-21244, RRID: AB_2535812), anti-mouse Alexa Fluor 488 dye-conjugated (Invitrogen A-11029, RRID: AB_2534088), anti-mouse Alexa Fluor 568 dye-conjugated (Invitrogen A-11004, RRID: AB_2534072), and anti-rat Alexa Fluor 568 dye-conjugated (Invitrogen A-11077, RRID: AB_141874), and they were used at a 1:500 dilution. For CK19 immunofluorescence, biotin-conjugated anti-rat antibodies and FITC-conjugated streptavidin were used. DNA was stained with DAPI contained within the ProLong Diamond Antifade mounting medium (Thermo Fisher Scientific).

For IHC, primary antibodies against αSMA (0.03 μg/mL; Abcam, ab7817, RRID: AB_262054), CDH1 (1:1,000; Cell Signaling Technology, 3195, RRID: AB_2291471), CK19 (1:35; DSHB, 2133570, RRID: AB_2133570), cleaved caspase-3 (1:1,000; Cell Signaling Technology, 9664, RRID: AB_2070042), and Ki-67 (1:100; clone SP6; Invitrogen, MA5-14520) were used.

Brightfield and immunofluorescence images were acquired at ambient temperature using a Plan-Apochromat 20×/0.8 M27 objective mounted on a ZEISS Axio Observer.Z1/7 microscope equipped with AxioCam 506 color camera and AxioCam 702 mono cameras. Polarized light images were acquired using a ZEISS Axioscan 7 Digital Slide Scanner (RRID: SCR_027284). Acquired pictures were subsequently analyzed using ImageJ/Fiji software (RRID: SCR_003070/RRID: SCR_002285) or QuPath (RRID: SCR_018257). The "Directionality" ImageJ plugin was used to infer the preferred orientation of collagen fibers in the picrosirius red polarized input images. All quantifications were performed on at least three random pictures. Analyzed images were carefully reviewed to exclude artifacts and false positives. Immunostainings for αSMA on human PDAC tissues were carefully checked and analyzed by a board-certified pathologist.

Immunoblotting

Total protein extracts were prepared in RIPA lysis buffer supplemented with protease and phosphatase inhibitors (Roche) and subjected to electrophoresis on SDS/PAGE. The separated proteins were transferred onto polyvinylidene difluoride membranes (Millipore) by electroblotting. Primary antibodies against ACT1B (1:1,000; Santa Cruz Biotechnology, sc-47778, RRID: AB_626632), ACTN4 (1:1,000; Abcam, ab108198, RRID: AB_10858236), ATM (1:1,000; Abcam, ab32420, RRID: AB_725574), GAPDH (1:1,000; Cell Signaling Technology, 2118, RRID: AB_561053), KEAP1 (1:1,000; Cell Signaling Technology, 8047, RRID: AB_10860776), PXN (1:1,000; clone 5H11; Invitrogen, AHO0492), and TGFβ1 (1:1,000; Abcam, ab215715, RRID: AB_2893156) were used. The second antibodies were anti-mouse IgG, horseradish peroxidase (HRP)–linked whole antibodies (from sheep; Amersham ECL, NA931), and anti-rabbit IgG, HRP-linked whole antibodies (from donkey; Amersham ECL, NA934), both used at a 1:5,000 dilution.

Flow cytometry on CAFs

For isolating cancer cells and CAFs, AKPC and KPC tumors were processed as previously described (24). CAFs were sorted using the mouse Tumor-Associated Fibroblast Isolation Kit (Miltenyi Biotec) according to the manufacturer's protocol. For flow cytometric analyses, cells were fixed in cold 4% formaldehyde, permeabilized with 90% methanol at 4°C for 15 minutes, and incubated with antibodies for 30 minutes. Antibodies used were anti-αSMA (1:1,000; Abcam, ab7817, RRID: AB_262054) and anti-mouse Ly6C-APC-eFluor780 (0.5 μg/reaction; clone HK1.4; Invitrogen, 17.5932.82). The secondary antibody was anti-mouse Alexa Fluor 488 dye–conjugated (1:500; Invitrogen, A110291). Cells were sorted on an Attune NxT Flow Cytometer (Thermo Fisher Scientific, RRID: SCR_019590).

qPCR

Total RNAs were extracted using the RNeasy Mini Kit (QIAGEN). First-strand complementary DNA (cDNA) was synthesized from 250 ng of RNA using SuperScript II Reverse Transcriptase and random primers (Thermo Fisher Scientific) according to the manufacturer's protocol. qPCR was performed using a QuantStudio 3 Real-Time PCR System (RRID: SCR_018712; annealing temperature 60°C) and PowerUp SYBR Green Master Mix (Thermo Fisher Scientific). All the real-time values were averaged and compared using the threshold cycle (CT) method, in which the amount of target RNA ($2^{-\Delta\Delta CT}$) was normalized to the endogenous expression of *18S* (ΔCT). The amount of target mRNA in control cells was set as the calibrator at 1.0. Primers used for qPCR were purchased from Sigma-Aldrich (KiCqStart SYBR Green Primers: *ACTA2*, *CXCL12*, *IL6*, *PDGFRA*, *PDGFRB*, and *POSTN*; *Acta2*, *Cxcl1*, *Il11*, *Il6*, *Postn*, *Pdgfrb*, and *Tagln*) and Biomers (*18S*: Fw: 5′-GTAACC

Downloaded from http://aacrjournals.org/cancerres/article-pdf/doi/10.1158/0008-5472.CAN-26-0138/3803456/can-26-0138.pdf by DKFZ - German Cancer Research Center user on 25 June 2026

CGTTCCCATT-3′, Rev: 5′-CCATCCAATCGTAGCG-3′; *CTGF*: Fw: 5′-CCTGGTCCAGACCACAGAGT-3′, Rev: 5′-TGGAGATTTTGGGAGTACGG-3′; *CXCL2*: Fw: 5′-TGCAGGGAATCTCAAG-3′, Rev: 5′-TGAGACAAGCTGCCCA-3′; mouse *18S*: Fw: 5′-GTAACCCGTTCCCATT-3′, Rev: 5′-CCATCCAATCGTAGCG-3′; and mouse *Tgfb1*: Fw: 5′-TGGAGCAACATGTGGAACTC-3′, Rev: 5′-GTCAGCAGCCGGTTACCA-3′).

Sample collection and processing for single-cell analyses

PDAC tumors were harvested from two female KPC and two female AKPC mice and snap-frozen. Twenty to thirty milligrams of tissue samples were resuspended in 1 mL of wash buffer (0.25 mol/L sucrose, 25 mmol/L KCl, 5 mmol/L $MgCl_2$, 10 mmol/L Tris-HCl (pH 7.5), 1 mmol/L DTT (Sigma-Aldrich, D9779), 1× protease inhibitor (Thermo Fisher Scientific, PIA32965), 1 U/μL recombinant RNasin (Promega, PAN2515), and 0.1% IGEPAL (Sigma-Aldrich, I8896) in molecular biology water) and then homogenized using a Dounce homogenizer with two pestles. First, a loose pestle was used for 5 to 10 strokes to break the tissue into small pieces, and then a tight pestle was used for 15 to 25 strokes to fully homogenize the sample into a uniform solution. Homogenized tissue was filtered through a 30 μm filter (CellTrics, Sysmex) and then centrifuged with a swinging-bucket centrifuge (100 rcf, 10 minutes, 4°C, Eppendorf, 5920 R). Nuclei were resuspended in 1 mL of wash buffer [0.25 M sucrose, 25 mmol/L KCl, 5 mmol/L $MgCl_2$, 10 mmol/L Tris-HCl (pH 7.5), 1 mmol/L DTT (Sigma-Aldrich, D9779), 1× protease inhibitor (Thermo Fisher Scientific, PIA32965), 1 U/μL recombinant RNasin (Promega, PAN2515) in molecular biology water] and centrifuged again (100 rcf, 10 minutes, 4°C, Eppendorf, 5920 R). Next, nuclei were resuspended in 400 μL of sorting buffer [1× protease inhibitor (Thermo Fisher Scientific, PIA32965), 1 U/μL recombinant RNasin (Promega, PAN2515), 1% fatty acid-free BSA (ProLiant, 7500804), and 2 μmol/L 7-AAD (Invitrogen, A1310) in PBS (Corning, 21-040-CV)] and incubated on ice for 10 minutes. In total, 120,000 nuclei were sorted into a LoBind tube with 90 μL collection buffer (5 U/μL recombinant RNasin (Promega, PAN2515), 5% fatty acid-free BSA (ProLiant, 7500804) in PBS (Corning, 21-040-CV) using an SH800 cell sorter (Sony). The resulting nuclei suspension was centrifuged again (500 rcf, 5 minutes, 4°C, Eppendorf, 5920 R) and resuspended in 100 μL of collection buffer [1% fatty acid–free BSA (ProLiant, 7500804), 1× protease inhibitor (Thermo Fisher Scientific, PIA32965), 10 mmol/L Tris-HCl (pH 7.4), 0.1% Tween-20 (Sigma-Aldrich, P7949-100ML), 0.1% IGEPAL (Sigma-Aldrich, I8896), 0.01% digitonin (Promega, G9441), 1 mmol/L DTT (Sigma-Aldrich, D9779), 1 U/μL recombinant RNasin (Promega, PAN2515), 3 mmol/L $MgCl_2$, and 10 mmol/L NaCl in molecular biology water]. This suspension was incubated on ice for 1 minute and centrifuged again (500 rcf, 5 minutes, 4°C, Eppendorf, 5920 R). The supernatant was carefully removed without disturbing the pellet, and 10 μL of 1× Nuclei Buffer (10x Genomics) was used to gently resuspend the pellet. Nuclei were counted using a hemocytometer, and approximately 20,000 nuclei were used as inputs for the tagmentation reaction.

Paired single-nucleus RNA sequencing and Assay for Transposase-Accessible Chromatin using sequencing

Nuclei from the two KPC mice were pooled together, and nuclei from the two AKPC mice were also pooled together, for a total of two sets of libraries. Then, single-cell multiome Assay for Transposase-Accessible Chromatin (ATAC) and gene expression libraries were generated according to the manufacturer's instructions (Chromium Next GEM Single Cell Multiome ATAC + Gene Expression Reagent Bundle, 10x Genomics, 1000283; Chromium Next GEM Chip J Single Cell Kit, 10x Genomics, 1000234; Dual Index Kit TT Set A, 10x Genomics, 1000215; and Single Index Kit N Set A, 10x Genomics, 1000212). The following PCR cycles were used: 7 cycles for ATAC index PCR, 7 cycles for cDNA amplification, and 13 to 16 cycles for RNA index PCR. A Qubit fluorometer (Life Technologies) was used to quantify the final libraries, and a TapeStation (High Sensitivity D1000, Agilent Technologies) was used to check size distribution. Finally, libraries were sequenced on the Illumina NextSeq 500 (RRID: SCR_014983) and the Illumina NovaSeq 6000 Sequencing System (RRID: SCR_016387) with the following read lengths (Read1 + Index1 + Index2 + Read2): ATAC (NovaSeq 6000), 50 + 8 + 24 + 50; ATAC (NextSeq 500 with custom recipe), 50 + 8 + 16 + 50; and RNA (NextSeq 500, NovaSeq 6000), 28 + 10 + 10 + 90.

Paired single-nucleus RNA sequencing and ATAC using sequencing data quantification and alignment

Raw FASTQ files from both libraries were processed with the 10x Genomics Cell Ranger ARC v2.0.0 (RRID: SCR_023897) count command. This command aligned all reads to the mm10 mouse genome reference and created BAM files and raw feature barcode matrices for both single-nucleus RNA (snRNA) and single-nucleus ATAC (snATAC).

Paired snRNA sequencing and ATAC using sequencing quality control and doublet identification

First, barcodes associated with empty droplets or multiplets—droplets with multiple barcodes and only one nucleus found by Cell Ranger ARC count—were identified and removed. Barcodes were considered empty droplets if they had less than or equal to 500 unique RNA genes with counts or less than or equal to 1,000 unique ATAC fragments. To retain only data from high-quality barcodes, additional filters were applied. Barcodes were removed if they had RNA percent mitochondrial reads greater than 5% or equal to or more than 5,000 ATAC mitochondrial reads. These counts from background contamination were removed from the snRNA sequencing (snRNA-seq) counts matrix using SoupX v1.6.2 (RRID: SCR_019193). SoupX identifies genes composing the background from empty droplets, uses these to estimate the proportion of contamination per barcode, and then lowers counts associated with all background genes for each cell.

Doublets were identified using Scrublet v0.2.3 (RRID: SCR_018098) on each library separately. Scrublet creates simulated doublet signatures using the input data clusters and then calculates a per-barcode doublet likelihood score based on the similarity to synthetic doublets. Scrublet was run on each library separately with an expected doublet rate of 0.06. All barcodes with a Scrublet doublet likelihood score above 0.25 were considered doublets and removed. After removing low-quality barcodes and doublets, 10,404 high-quality cells remained from both libraries.

Paired snRNA-seq and ATAC using sequencing dimensionality reduction and clustering

Before dimensionality reduction and clustering, all snATAC using sequencing (snATAC-seq) fragments were quantified across 5 kb regions tiling the genome to create a window-based count matrix. Seurat v4.3.0 (RRID: SCR_016341) and Signac v1.10.0 (RRID: SCR_021158) were used to perform all subsequent analyses. First, data normalization and dimensionality reduction were performed on the snRNA and snATAC data separately. snRNA-seq counts were

Downloaded from http://aacrjournals.org/cancerres/article-pdf/doi/10.1158/0008-5472.CAN-26-0138/3803456/can-26-0138.pdf by DKFZ - German Cancer Research Center user on 25 June 2026

normalized using SCTransform v0.4.0 (RRID: SCR_022146), reduced to principal components (PC) with principal component analysis (PCA), and then projected into two-dimensional space using Uniform Manifold Approximation and Projection for Dimension Reduction (UMAP, RRID: SCR_018217; arXiv 1802.03426) on the top 50 PCs. snATAC-seq counts were normalized with Term Frequency-Inverse Document Frequency, Single Value Decomposition was used to perform dimensionality reduction, and then the top 2 through 50 dimensions were used to run UMAP. The single top dimension was excluded, as it usually correlates with sequencing depth. Seurat's weighted nearest neighbor (34) clustering was used to combine information from both assays into one dimensionality reduction map. The FindMultiModalNeighbors command was run using the top 50 RNA dimensions and the top 2 through 50 ATAC dimensions. Then, UMAP was run, and clustering was performed with the Leiden algorithm and a resolution of 0.5. Both libraries were dimensionality reduced and clustered separately first to ensure they were of good quality and then integrated together using Harmony v1.0.1 (RRID: SCR_018809) batch correction and reanalyzed following the same methods.

Assignment of cell type identities

Cell types were identified by the cluster-specific expression of known marker genes for PDAC tumors. We used previously characterized (14, 35) mouse marker genes to classify the following cell types: acinar cells (*Ctrb1*), B cells (*Bank1*), dendritic cells (*Cacnb3*), ductal cells (*Prom1*), endothelial cells (*Egfl7*), myeloid cells (*Adgre1*), perivascular cells (*Rhoj*), T and NK cells (*Il17r*), and CAFs (*Dcn*). To identify known subtypes of ductal cells and CAFs, the cells from each cell type were reclustered separately using a resolution of 0.5. Epithelial-to-mesenchymal transition (EMT)–like cells, a subtype of ductal tumor cells expressing markers of the EMT, were classified by the expression of *Hmga2*. Previously identified CAF subpopulations were also detected after subclustering all fibroblasts: myCAFs (*Col12a1*, *Tnc*, and *Col8a1*), iCAFs (*Scep1*, *Plpp3*, and *Scara5*), and apCAFs (*Ptgis*, *Fth1*, and *Cxadr*).

Analysis of lymphoid and myeloid cells

To identify subpopulations of lymphoid and myeloid cells, cell barcodes annotated as B cells, T and NK cells, or myeloid cells were subset and reanalyzed using optimized parameters. snRNA-seq counts were normalized using SCTransform (RRID: SCR_022146), regressing out mitochondrial reads. The top 2000 variable features were used for linear dimensionality reduction with PCA, followed by batch correction with Harmony (RRID: SCR_018809) and projection into UMAP space using the top 17 (lymphoid)/21 (myeloid) harmony-corrected PCs. snATAC-seq peaks with 0 counts across remaining cells were removed; counts were normalized using TF-IDF before linear dimensionality reduction using SVD and batch integration with Harmony. The top two through six harmony-corrected Latent Semantic Indexing dimensions were used for UMAP embedding of the snATAC-seq data. RNA and ATAC modalities were integrated through the weighted nearest-neighbor (34) approach with 20 k-nearest neighbors. Clustering was performed using the Leiden algorithm at a resolution of 0.7 (lymphoid)/0.5 (myeloid). Lymphoid subtypes were annotated based on the expression of canonical marker genes: B cells (*Bank1*, *Pax5*, and *Ebf1*), $CD4^+$ T cells (*Il7r*, *Cd3g*, and *Cd4*), $CD8^+$ T cells (*Il7r*, *Cd3g*, *Cd8a*, and *Cd8b1*), Tregs (*Il7r*, *Cd3g*, *Cd4*, *Foxp3*, and *Ctla4*), and NK cells (*Klrb1b*, *Klrk1*, and *Gzma*). Myeloid clusters were annotated based on previously defined marker gene signatures (36) and signature marker genes: M1-like tumor-associated macrophages (TAM; *Cd80*, *H2-Aa*, and *H2-Ab1*), M2-like TAMs (*Arg1* and *Fn1*), phagocytotic TAMs (*Mrc1* and *Cd163*), and proliferating TAMs (*Mki-67* and *Top2a*).

Identification of cell type peaks from snATAC-seq data

Regions of accessible chromatin consistently found in each cell type were identified by peak calling with MACS2 (RRID: SCR_013291). Cell type pseudobulk profiles were assembled by combining the fragments for all barcodes assigned to each cell type. Cell types with more than 100 million total fragments were randomly downsampled to 100 million fragments, and then the MACS2 (v2.2.7.1) callpeak tool was used to identify peaks with a false discovery rate (FDR) of less than 0.05. Duplicate peaks were retained. All cell type peaks were merged into an overall peak list using BEDTools (RRID: SCR_006646) merge. ATAC fragments for each merged peak were quantified by barcode and used to create an snATAC-seq peak-based count matrix. Finally, all peaks were reduced to a fixed width of 500 bps around the peak summit.

Identification of genes and pathways differing between genotypes and cell types

Seurat's findMarkers function was used to identify genes and accessible chromatin peaks that differed between cells within a cell type from each genotype (KPC and AKPC). A Wilcoxon rank-sum test was used to compare the gene and peak counts from both groups, and Bonferroni multiple test correction was performed to identify significant changes. For the differentially expressed genes from snRNA-seq data, gene set enrichment was performed using fGSEA v1.28.0 (bioRxiv 060012). First, the differential expression rank of each gene was calculated by multiplying the negative $\log_{10}$ P value of the difference by the $\log_2$ fold change. All genes with a rank of 0 were assigned a pseudocount of the minimum positive nonzero rank value. Then, fGSEA was performed on the rank stats for all pathways with less than 500 genes from the following pathway sets from mSigDB (RRID: SCR_016863) mm10 database: MH (orthology-mapped hallmark gene sets), M5 Gene Ontology (GO; ontology gene sets, GO), and M2 CP:Reactome (curated gene sets, real-time gene sets). All pathways with a Benjamini–Hochberg adjusted P value less than 0.1 were considered significantly different between genotypes. To assess the enrichment of predefined gene signatures in different cell types, Seurat's AddModuleScore function was used.

Creation of genotype-specific CAF subtype trajectories using gene expression

The Monocle3 package v1.3.4 (RRID: SCR_018685) was used to perform gene expression-based trajectory analysis of CAF subtypes for both the KPC and AKPC genotypes separately. For each genotype, a cell dataset object was constructed using the raw RNA counts from all CAF cells, and then the top 100 dimensions from PCA were used to reduce the dimensionality using the UMAP method with 10 nearest neighbors and a minimum distance of 0.01. Cells were clustered using the Louvain algorithm, 40 nearest neighbors, and a partition q value of 0.01. Finally, the trajectory was learned by using Monocle's learn_graph function, with an additional loop-closing step, only learning a single graph across all partitions and with up to three layers of nearest neighbor trees.

Prediction of cell–cell signaling interactions

CellChat v1.6.1 (RRID: SCR_021946) was used to predict cell–cell signaling interactions between all cell types from scRNA-seq count

Downloaded from http://aacrjournals.org/cancerres/article-pdf/doi/10.1158/0008-5472.CAN-26-0138/3803456/can-26-0138.pdf by DKFZ - German Cancer Research Center user on 25 June 2026

data of known genes for ligands and receptors. CellChat was run on each library separately using the CellChatDB mouse reference of known ligand and receptor signaling pairs involved in secreted signaling. The probability of interactions between cell types was calculated using average cell type gene expression, with bootstrapping to calculate *P* values for each predicted interaction. After filtering out interactions between small numbers of cells, communication was aggregated into signaling pathways and summarized. Next, to compare signaling interactions between the two genotype libraries, the two CellChat objects were merged. The number of interactions and overall interaction strength per pathway were compared, as well as the amount of incoming and outgoing signals per cell type and genotype. Finally, latent communication patterns of coordinated pathways across cell types were calculated using CellChat's nonnegative matrix factorization method.

Integrated analysis of transcription factor motif accessibility and target gene expression

Transcription factor (TF)–target regulatory relationships were obtained from the TRRUST v2.0 (RRID: SCR_022554) and ORegAnno v3.0 (RRID: SCR_007835) databases. Mouse TFs with at least seven target gene counts (activated, repressed, or both) were selected for the analysis. Position weight matrices of TF-binding motifs were obtained from the vertebrate CORE collection of the JASPAR 2020 database (RRID: SCR_003030). Enrichment scores of motifs in accessible regions were calculated for each cell using chromVAR (RRID: SCR_026570) through the Signac function RunChromVAR().

Differential accessible TF-binding motifs within each cell type from both AKPC and KPC genotypes were identified using the Wilcoxon rank-sum test implemented in Seurat's FindAllMarkers() function with Bonferroni multiple test correction. All motifs with an adjusted *P* value smaller than 0.05 were considered significantly enriched. Similarly, Seurat's FindAllMarkers() function was used with a Wilcoxon rank-sum test to identify differentially expressed genes between cell types from both genotypes. The differential expression rank for each gene was calculated by multiplying the negative $\log_{10}$ *P* value by the sign of the $\log_2$ fold change.

To identify TFs displaying both significant motif and target gene enrichment in a specific cell type, a readout for predicted TF activity, gene set enrichment analysis (GSEA) was performed on the target genes of the TFs that were enriched in a cell type from either AKPC or KPC or both genotypes using GSEA in preranked mode. Statistical significance for target gene enrichment was set at a *P* value cutoff of 0.05. Running enrichment scores for leading edge genes were normalized by gene set size.

Bulk RNA-seq

Library preparation for bulk 3′-sequencing of poly(A)-RNA was done as described previously (37). Briefly, barcoded cDNA of each sample was generated with Maxima Reverse Transcriptase polymerase (Thermo Fisher Scientific) using an oligo-dT primer containing barcodes, unique molecular identifiers (UMI), and an adapter. The 5′ ends of the cDNAs were extended by a template switch oligo (TSO); after pooling all samples, full-length cDNA was amplified with primers binding to the TSO site and the adapter. cDNA was tagmented with the Nextera XT kit (Illumina), and 3′ end fragments were finally amplified using primers with Illumina P5 and P7 overhangs. In comparison with Parekh and colleagues (37), the P5 and P7 sites were exchanged to allow sequencing of the cDNA in read1 and barcodes and UMIs in read2 to achieve better cluster recognition. The library was sequenced on an Illumina NextSeq 500 (RRID: SCR_014983) with 75 cycles for the cDNA in read1 and 16 cycles for the barcodes and UMIs in read2. Gencode gene annotations version M18 and the mouse reference genome major release GRCm38 were derived from Gencode (RRID: SCR_014966). Drop-seq tools v1.12 were used for mapping the raw sequencing data to the reference genome. The resulting UMI-filtered count matrix was imported into R v3.4.4 (RRID: SCR_001905). Prior to differential expression analysis with DESeq2 1.18 (RRID: SCR_015687), the dispersion of the data was estimated with a parametric fit, including the treatment the cell lines underwent as an explanatory variable in the model. The Wald test was used to determine differentially regulated genes between the treated and nontreated groups, and shrunken $\log_2$ fold changes were calculated afterward, with the type argument of the lfcShrink function set to normal. A gene was determined to be differentially regulated if the absolute $\log_2$ fold change was greater than 0.848 or lower than −0.848, and the adjusted *P* value was below 0.05. GSEAs were performed using R v3.4.4 (RRID: SCR_001905).

Proteomics sample preparation

Tumor cells were seeded in DMEM containing 10% FBS and P/S and propagated until reaching 70% confluency. The medium was replaced with serum-free DMEM containing P/S, and the cells were propagated for an additional 24 hours before cell harvesting. Cell pellets were washed using cold 1× PBS and spun down at 4°C. Cell pellets were snap-frozen using liquid nitrogen prior to −80°C storage and processing. Cell pellets were lysed in 8 mol/L urea, 100 mmol/L NH_4HCO_3, and 1 mmol/L DTT (pH 8.0). The total protein content of the cell lysate was determined using the BCA Protein Assay Kit (Thermo Fisher Scientific). Two hundred micrograms of total protein per sample was reduced (10 mmol/L DTT, 30 min at 30°C), alkylated (55 mmol/L chloroacetamide, room temperature, 30 min, in the dark), and diluted to 1.3 M urea with 50 mmol/L NH_4HCO_3. Protein digestion was performed by adding trypsin (Trypsin Gold Mass Spectrometry Grade, Promega, 1:50 enzyme-to-substrate ratio) and incubating overnight at 37°C. Digests were acidified with 1% formic acid (FA) and desalted using 50 mg tC18 reversed-phase (RP) solid-phase extraction cartridges (Sep-Pak, Waters, WAT054960). Peptide solutions were dried and frozen at −80°C until Tandem Mass Tag labeling.

TMT labeling and offline peptide fractionation

In total, 10 samples were analyzed, including 5 biological replicates of KPC and AKPC cell lines. The 10 samples were measured in a TMT11-plex experiment, together with one pooled sample. TMT11-plex labeling was carried out according to Zecha and colleagues (38). Briefly, peptide solutions (200 µg protein amount per sample) were reconstituted in 20 µL of 100 mmol/L HEPES buffer (pH 8.5). Next, TMT11-plex reagents (Thermo Fisher Scientific) in 100% anhydrous acetonitrile were added in a final concentration of 11.6 mmol/L to all peptide samples. After incubation for 1 hour at 25°C and 400 rpm, the labeling reaction was stopped by adding 2 µL of 5% hydroxylamine (15 minutes, at 25°C and 400 rpm). The 11 peptide samples were pooled and dried down. Subsequently, they were desalted using 500 mg tC18 RP solid-phase extraction cartridges (Sep-Pak, Waters, WAT020805), dried, and frozen at −80°C. Finally, the TMT11-plex experiment was off-line fractionated using basic reverse phase chromatography. Briefly, 150 µg of peptides were reconstituted in 25 mmol/L ammonium bicarbonate (pH 8.0) and loaded onto a C18 column (XBridge BEH 130, 3.5 µm, 2.1 × 150 mm, Waters Corp.). Peptides were eluted with increasing

Downloaded from http://aacrjournals.org/cancerres/article-pdf/doi/10.1158/0008-5472.CAN-26-0138/3803456/can-26-0138.pdf by DKFZ - German Cancer Research Center user on 25 June 2026

acetonitrile concentration to yield 96 fractions, which were subsequently pooled into 32 fractions. All fractions were dried down before LC/MS-MS analysis.

LC/MS-MS measurements

Nano-flow LC/MS-MS measurements of the TMT-labeled peptides were performed on a Thermo Scientific Fusion Lumos Tribrid mass spectrometer (RRID: SCR_020562) equipped with an UltiMate 3000 RSLCnano system (RRID: SCR_026145). For each analysis, peptides were delivered to a trap column (ReproSil-Pur C18-AQ, 5 μm, Dr. Maisch, 20 mm × 75 μm, self-packed) at a flow rate of 5 μL/min in 100% solvent A (0.1% FA in high-performance liquid chromatography grade water). After 10 minutes of loading, peptides were transferred to an analytic column (ReproSil Gold C18-AQ, 3 μm, Dr. Maisch, 450 mm × 75 μm, self-packed with a self-pulled tip using a Laser-Pipette-Puller P-2000) and separated using a 50 min gradient from 8% to 32% of solvent B [0.1% FA in acetonitrile and 5% (v/v) DMSO] at a flow rate of 300 nL/min. Both nanoLC solvents contained 5% DMSO (v/v). The Fusion Lumos was operated in data-dependent acquisition, positive ionization, and multinotch MS3 mode. Full scan MS1 spectra were recorded over a range of 360 to 1,500 m/z at a resolution of 60k using an automatic gain control (AGC) target value of 4e5 and a maximum injection time of 50 milliseconds. Precursor ions were filtered according to charge state (2–6), dynamic exclusion (60 seconds with a ±10 ppm window), and monoisotopic precursor selection. MS2 spectra were recorded in the Orbitrap at 30K resolution and with a quadrupole isolation window of 0.7 m/z (scan range mode: Auto:m/z Normal). Fragmentation was performed with collision-induced dissociation and a normalized collision energy (NCE) of 35% (AGC target value 5e4, maximal injection time 60 milliseconds). For TMT reporter ion quantification, an additional MS3 spectrum was acquired in the Orbitrap over an m/z range of 100 to 1,000 at 50k resolution. For this, fragment ions were selected by multinotch isolation, allowing a maximum of 10 notches. MS1 precursor isolation was set to 0.7 m/z, whereas the MS2 isolation window width was set to 2 m/z. Fragmentation in the Orbitrap was performed by HCD at 55% NCE (AGC target value 1e5, maximal injection time 120 milliseconds). The overall cycle time of the method was 3 seconds.

MaxQuant database searching

Peptide identification and quantification were performed using MaxQuant v1.6.17.0 (RRID: SCR_014485) with its built-in search engine Andromeda. Raw files were searched against the UniProt mouse reference database (downloaded from UniProt in July 2020, 55,462 protein entries) supplemented with common contaminants. MS3-based TMT quantification was enabled. For all searches, carbamidomethylated cysteine was set as a fixed modification, and oxidation of methionine and N-terminal protein acetylation were set as variable modifications. Trypsin/P was specified as the proteolytic enzyme with up to two missed cleavage sites. Precursor tolerance was set to ±4.5 ppm, and fragment ion tolerance to ±20 ppm. Results were adjusted to a 1% FDR on peptide spectrum match and protein level, employing a target-decoy approach using reversed protein sequences.

Proteomic data normalization and statistical analysis

Before statistical analysis, we first $\log_{10}$-transformed and median-centered the protein intensity in each TMT channel to remove the potential influence resulting from different sample loading amounts. Next, we used the Student *t* test to identify proteins that were significantly differentially expressed between experimental conditions. All analyses were performed using R v4.1.2 (RRID: SCR_001905).

Secretome analysis on antibody microarrays

Antibody microarrays were produced and used as described (39). Briefly, antibodies were spotted onto epoxy-coated slides (NEXTERION-E; Schott) using a MicroGrid-2 contact printer (BioRobotics) with SMP3B pins (Telechem). A common protein reference sample made from 24 pancreatic cancer cell lines (40) was incubated on a microarray in parallel. The reference provided information about experimental performance and allowed direct data normalization. The protein concentration of secretome and reference samples was adjusted to 4.0 mg/mL. Labeling was conducted using the fluorescent dyes DY649 or DY549 (Dyomics), respectively, at a molar protein/dye ratio of 7.5 in PBS (pH 7.2) at 4°C for 2 hours. Subsequently, 10% glycine in PBS was added to quench unreacted dye. For analyses, the microarray surface was blocked with 10% nonfat dry milk in TBS and 0.05% Tween 80 for 3 hours at room temperature. The blocked slides were incubated with 25 μg/mL each of labeled secretome sample and common reference at 4°C overnight. After washing, a PowerScanner system (Tecan) was used for image capture at constant laser power and photomultiplier tube gain. Image analysis was performed with GenePix Pro 6.0 software (Molecular Devices), generating numerical values of signal intensities. The data were analyzed using R v4.0.4 (RRID: SCR_001905). The Loess method of the limma package (RRID: SCR_010943) was applied for data normalization with background correction offset (v3.50.1); variations were corrected by applying the functions "normalizeWithinArrays" and "normalizeBetweenArrays." An empirical Bayes test with Bonferroni–Hochberg adjustment was used for multiple testing.

Protein term enrichment analysis

Protein term enrichment analyses were conducted using the annotation tool DAVID (RRID: SCR_001881) with the BioCarta Pathways (RRID: SCR_006917), GO (RRID: SCR_002811), Kyoto Encyclopedia of Genes and Genomes (RRID: SCR_012773), Reactome (RRID: SCR_003485), and UniProt (RRID: SCR_002380) datasets. Significant enrichments are defined with $P < 0.05$.

Orthotopic assay

For syngeneic orthotopic transplantations, KC, AKC, KPC, and AKPC mouse tumor cells were implanted by an injection of 25×10^3 cells in 100 μL of 1:1 serum-free DMEM:Matrigel GFR into the pancreas of 8-week-old male C57BL/6J mice ($n = 5$ per condition). Tumor take was ≥72% for each cell line. Overall survival was calculated as the time elapsed between orthotopic transplantation and euthanasia at a predefined ethical endpoint. For xenogeneic orthotopic transplantations, CRISPR-edited hPANC cells and PDOs were implanted by an injection of 25×10^3 cells in 100 μL of 1:1 serum-free DMEM:Matrigel GFR into the pancreas of 8-week-old female Hsd:Athymic Nude-*Foxn1*^{nu} mice ($n = 6$ per condition). Tumor take was ≥90% across models. Overall survival was calculated as the time elapsed between treatment/enrollment start and euthanasia at a predefined ethical endpoint. The solutions of galunisertib (TGFBR1 inhibitor, 12.5 mg/kg) and FOLFIRINOX (leucovorin, 50 mg/kg; 5-fluorouracil, 25 mg/kg; irinotecan, 25 mg/kg; and oxaliplatin, 2.5 mg/kg) were administered by i.p. injection. Briefly, the treatment administration schedule was as follows: i.p. FOLFIRINOX injections every third day and i.p. galunisertib

Downloaded from http://aacrjournals.org/cancerres/article-pdf/doi/10.1158/0008-5472.CAN-26-0138/3803456/can-26-0138.pdf by DKFZ - German Cancer Research Center user on 25 June 2026

Downloaded from http://aacrjournals.org/cancerres/article-pdf/doi/10.1158/0008-5472.CAN-26-0138/3803456/can-26-0138.pdf by DKFZ - German Cancer Research Center user on 25 June 2026

injections every second day. Tumors were resected, fixed in cold 4% formaldehyde for 24 hours, and embedded in paraffin for histologic analysis.

Subcutaneous assay

For subcutaneous transplantation, tumor cells were implanted by subcutaneous injection of 4×10^5 KPC or AKPC tumor cells and 4×10^5 PSCs in 100 μL of 1:1 serum-free DMEM:Matrigel GFR into the flank of 7-week-old female Hsd:athymic nude-*Foxn1*^{nu} mice ($n = 8$ tumors per condition). Tumor take was 100% for all cell lines. The solutions of galunisertib (TGFBR1 inhibitor, 12.5 mg/kg) and MRTX1133 (Kras^{G12D} inhibitor, 3 mg/kg) were administered by i.p. injection. Briefly, the treatment administration schedule was as follows: MRTX1133 i.p. injections twice a day and i.p. galunisertib injections every second day. Tumors were resected, fixed in cold 4% formaldehyde for 24 hours, and embedded in paraffin for histologic analysis.

Patient-derived xenografts

For subcutaneous implantation, 4 mm^3 pieces of patient-derived xenografts (patient-derived *in vivo* expanded pancreatic tumors) were embedded in ECM Gel from Engelbreth–Holm–Swarm murine sarcoma (Sigma-Aldrich) and transplanted into the flank of 6- to 8-week-old female Hsd:athymic nude-*Foxn1*^{nu} mice. Tumor take was 100% for all patient-derived xenografts. Tumor size was measured 3 times a week with a caliper, and the tumor volumes were determined with the following equation: $v = (l \times w^2) \times \pi/6$ (where v is volume, l is length, and w is width). For each group, eight patient-derived xenografts were implanted. Tumors were randomized when the volume reached 50 to 100 mm^3 before starting treatment. The solutions of galunisertib (TGFBR1 inhibitor, 12.5 mg/kg) and FOLFIRINOX (leucovorin, 50 mg/kg; 5-fluorouracil, 25 mg/kg; irinotecan, 25 mg/kg; and oxaliplatin, 2.5 mg/kg) were administered by i.p. injection. Briefly, the treatment administration schedule was as follows: i.p. FOLFIRINOX injections every third day and i.p. galunisertib injections every second day. Mice were euthanized when tumors reached a maximal volume of 1,000 mm^3. Tumors were resected, fixed in cold 4% formaldehyde for 24 hours, and embedded in paraffin for histologic analysis.

Magnetic resonance imaging

Magnetic resonance (MR) imaging (MRI) was performed to assess tumor growth using a dedicated ultrahigh field 11.7T small animal system (BioSpec 117/16, Bruker Biospin) equipped with a 9-cm gradient insert (BGA-S9). MRI data were acquired using ParaVision 6.01 software (RRID: SCR_001964) with a four-channel receive-only surface coil placed anterior to the tumor area. Anesthesia was maintained using 1.5% isoflurane (AbbVie) and adjusted to maintain a safe respiration rate of about 60 cycles per minute. The imaging protocol comprised a multislice 2D RARE technique in coronal and axial slice orientation with acquisition parameters as follows: TE (echo time)/TR (repetition time) = 23 milliseconds/1,500 milliseconds, spatial resolution $\Delta r = 90 \times 90 \times 500$ μm^3, and RARE factor = 8. All MR images were analyzed using the ITK-SNAP software tool (RRID: SCR_002010), which allowed for accurate manual segmentation of the tumors in 3D.

Analysis of publicly available databases

Mutual co-occurrence and exclusivity of selected DDR gene mutations were assessed using the Fisher exact test. Bayesian cell type and gene expression deconvolution of The Cancer Genome Atlas (TCGA) bulk RNA-seq data were performed using BayesPrism (RRID: SCR_027499; ref. 41) with the Peng and colleagues dataset (42) as a single-cell reference. Raw single-cell count matrices and cell type annotations were obtained from GSA accession CRA001160. Doublet barcodes were marked using scDblFinder (RRID: SCR_022700) and removed from the analysis. Additional quality control filters were percent mitochondrial reads <30% and unique RNA genes between the 2.5th and 97.5th percentiles. scRNA-seq counts were log-normalized and scaled, regressing out percent mitochondrial reads and cell-cycle scores. Linear dimensionality reduction was performed using the top 3,000 variable features, followed by integration with Harmony (RRID: SCR_018809) and projection into UMAP space using the top 21 harmony-corrected PCs. Clusters were identified using the Louvain algorithm with 25 k-nearest neighbors at a resolution of 0.18. Cell type identities were assigned to each cluster by cross-referencing with the annotations from the original study (42). For the annotation of CAFs, fibroblasts and stellate cells were subset and reanalyzed using the same workflow with 2,000 variable features, 25 harmony-corrected PCs, 10 k-nearest neighbors, and a clustering resolution of 0.2. Fibroblasts were annotated as myCAF, iCAF, and non-CAF according to previously described marker gene signatures (14, 43). BayesPrism deconvolution (41) was run on protein-coding genes using default parameters, treating major cell type annotations as cell types and CAF annotations as cell states. Validation of the deconvolution approach was performed by using pseudobulk gene expression profiles as the bulk input and correlating estimated and true cell type and cell state abundances. Deconvoluted cell type–specific gene expression from the TCGA RNA-seq data was normalized using variance-stabilizing transformation (44). Gene signature enrichment was calculated through gene set variation analysis (GSVA; RRID: SCR_021058). Correlations between malignant gene expression levels and cell type/state abundances and GSVA enrichment scores were computed using Spearman and Pearson correlation analysis, respectively.

Statistical analysis

GraphPad Prism (RRID: SCR_002798) software was used for statistical analysis and graphical representation of the data. Statistical significance was tested using an unpaired Student t test. For survival comparisons, statistical significance was tested using the log-rank test. Correlation analyses were conducted using the Pearson correlation test. For comparing human PDAC case numbers, contingency tables were generated, and statistical significance was tested using the Fisher exact test. All tests were considered to be statistically significant when $P < 0.05$.

Results

ATM loss of function accelerates pancreatic tumorigenesis in the absence of P53

P53 plays critical roles in maintaining genetic stability (2). Consistent with the genomically unstable phenotype reported in mouse ATM-deficient PDAC [AKC; (6, 8, 24)], P53 levels were higher in AKC cells, suggesting a significant activation of the P53 checkpoint (**Fig. 1A–C**). To test whether P53 restrains the effects of ATM loss of function during pancreatic tumorigenesis, we introduced a floxed *Trp53* allele (P) into *Atm*$^{fl/fl}$ (A); *LSL-Kras*$^{G12D/+}$ (K); *Ptf1a*$^{Cre/+}$ (C) mice to generate the AKPC animals (**Fig. 1D**). Although *Trp53* status determined the survival corridor, additional *Atm* deletion significantly reduced survival in both genotypes

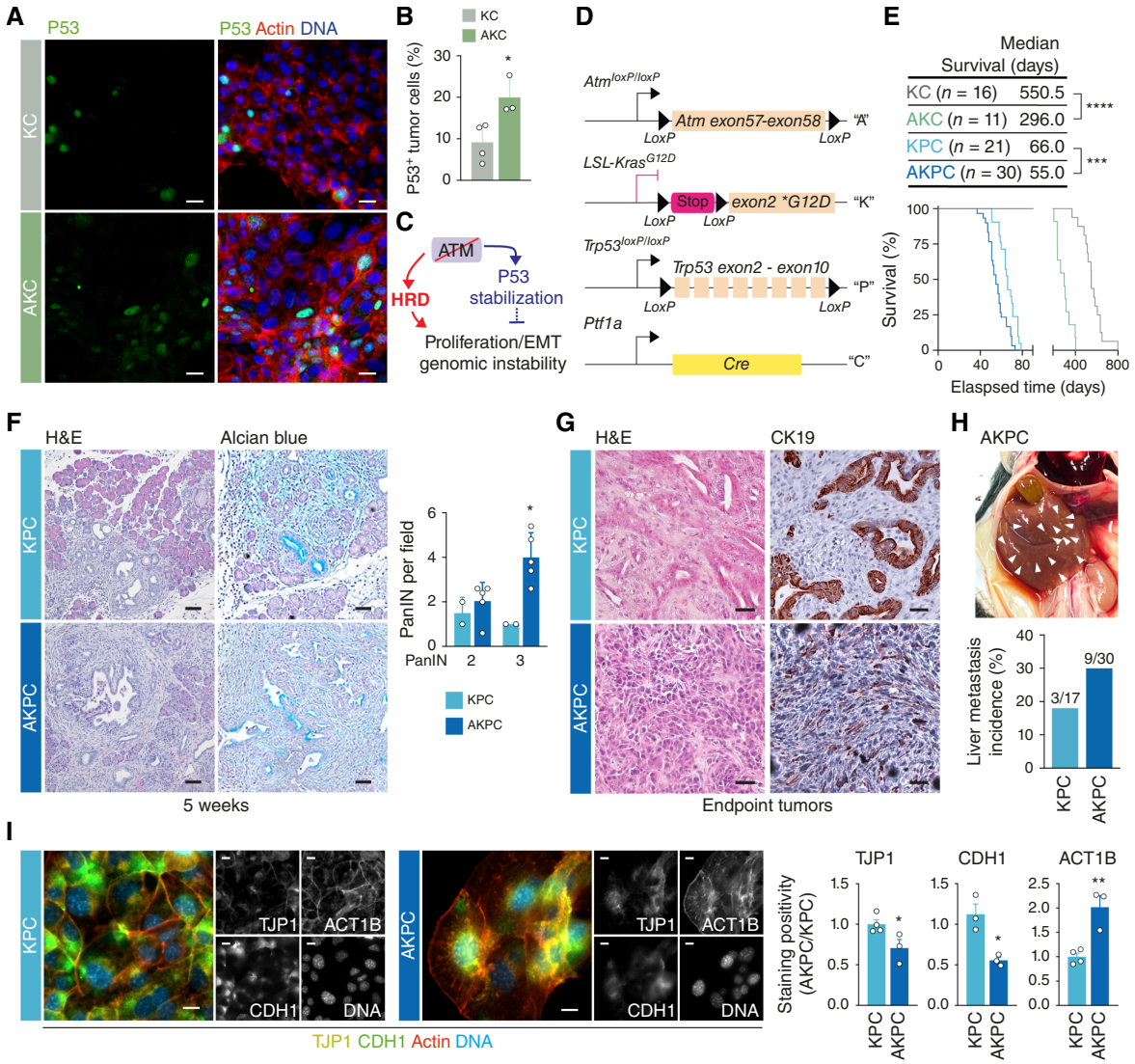


Figure 1.

ATM loss of function accelerates pancreatic tumorigenesis in a P53-deficient context. **A** and **B,** P53 immunofluorescence and phalloidin-Atto565 staining (cortical F-actin; **A**) and quantification of P53$^+$ cells in KC and AKC tumor cells (**B**). Nuclei were counterstained with DAPI. Scale bars, 20 μm. Mean ± SD of ≥3 cell lines/genotype (tested in ≥2 independent experiments); each dot represents a cell line. **C,** Schematic depicting the proposed impact of P53 on ATM loss-of-function–driven tumorigenesis. **D,** Schematic of *Ptf1a*^{Cre}, *LSL-Kras*^{G12D}, floxed *Atm*, and floxed *Trp53* alleles. **E,** Kaplan–Meier survival of KPC ($n = 21$), AKPC ($n = 30$), KC ($n = 16$), and AKC ($n = 11$) mice. **F,** H&E and alcian blue staining and quantification of pancreatic intraepithelial neoplasia (PanIN) lesions in 5-week-old KPC ($n = 2$) and AKPC ($n = 5$) mice. Scale bars, 100 μm. Mean ± SD; each dot represents a mouse. **G,** H&E staining and CK19 IHC in endpoint tumors. Scale bars, 50 μm. **H,** Representative image of liver metastases in an endpoint AKPC mouse and incidence in AKPC and KPC cohorts. Arrows indicate metastases. **I,** Immunofluorescence for TJP1 and CDH1 and phalloidin-Atto565 staining with quantification of TJP1$^+$, CDH1$^+$, and F-actin$^+$ surface normalized to nucleus count in KPC and AKPC malignant cells. Nuclei were counterstained with DAPI. Scale bars, 10 μm. Mean ± SD of ≥3 cell lines/genotype (tested in ≥2 independent experiments); each dot represents a cell line. **B, F,** and **I,** unpaired Student *t* test. **E,** Log-rank test. **H,** Fisher exact test. *, $P < 0.05$; **, $P < 0.01$; ***, $P < 0.001$; ****, $P < 0.0001$. H&E, hematoxylin and eosin.

(**Fig. 1E**). Heterozygous *Atm* loss also shortened survival in KPC mice, indicating a hypomorphic effect of the *Atm* allele (Supplementary Fig. S1A). Immunohistologic characterization revealed more frequent high-grade pancreatic intraepithelial neoplasia lesions in 5-week-old AKPC mice (**Fig. 1F**). At a later time point, ATM deletion led to invasive tumors with undifferentiated features, indicative of a mesenchymal and aggressive phenotype (**Fig. 1G**; Supplementary Fig. S1B). Liver metastasis tended to be more frequent in AKPC than in KPC counterparts (**Fig. 1H**). Isolated tumor cells also displayed prominent mesenchymal features upon ATM loss-of-function without detectable differences in proliferation (**Fig. 1I**; Supplementary Fig. S1C and S1D; refs. 6, 24). ATM is a central kinase in the DDR that safeguards against genomic instability (5). Accordingly, ATM-deficient malignant cells exhibited enlarged nuclei, indicative of aneuploidy, and higher DNA damage levels, even in the absence of the P53 checkpoint (Supplementary

Downloaded from http://aacrjournals.org/cancerres/article-pdf/doi/10.1158/0008-5472.CAN-26-0138/3803456/can-26-0138.pdf by DKFZ - German Cancer Research Center user on 25 June 2026

Downloaded from http://aacrjournals.org/cancerres/article-pdf/doi/10.1158/0008-5472.CAN-26-0138/3803456/can-26-0138.pdf by DKFZ - German Cancer Research Center user on 25 June 2026

Fig. S1E; refs. 5, 6). In sum, ATM deletion unleashes a mesenchymal dedifferentiation program in both P53-proficient KC (6, 24) and aggressive P53-deficient KPC cancers.

ATM-deficient tumor cells generate a myofibroblast-enriched TME

Immunostainings revealed modest immune alterations in ATM-deficient tumors, including reduced $B220^+$ and $B220^+CD11b^+$ populations but preserved $CD11b^+$, $Ly6C^+$, and $CD11b^+Ly6C^+$ myeloid and monocytic compartments, indicating selective loss of B-lineage cells and biphenotypic progenitors (Supplementary Fig. S2A). $CD3^+$ and $CD8^+$ T cells also showed a downward trend, together with a marked reduction in M2-like $CD206^+$ TAMs, suggesting an immunologically cold ecosystem. In contrast, ATM loss was associated with pronounced fibrosis in both P53-deficient and proficient contexts (**Fig. 2A**; Supplementary Fig. S2B). Collagen deposition comprised an increased collagen type I/III ratio, denoting a possible enrichment in collagen-producing αSMA^+ myCAFs (Supplementary Fig. S2C). Collagen fibers in AKPC tumors seemed more organized with increased directionality, a negative prognostic feature promoting EMT and dissemination (45), consistent with their invasive phenotype. αSMA immunoreactivity confirmed increased αSMA^+ fibroblasts in AKPC compared with KPC counterparts (**Fig. 2A**; Supplementary Fig. S2D). Concomitantly, SMAD2 phosphorylation and nuclear translocation in αSMA^+ myofibroblasts indicated the activation of canonical TGFβ signaling, supporting ATM loss-dependent TME remodeling toward a myCAF fate (21). This myofibroblastic programming was P53-independent, highlighting epithelial ATM status as a critical determinant of CAF differentiation. To resolve the stromal landscape of ATM-deficient PDAC, we performed single-nucleus multiomics (snRNA/snATAC) on KPC and AKPC tumors, following careful removal of adjacent lymph nodes (**Fig. 2B**). A total of 10,445 nuclei were sequenced (AKPC: 5,698, KPC: 4,747). After quality control, dimensionality reduction identified 13 cell clusters annotated by signature genes and lineage markers (**Fig. 2C**; Supplementary Fig. S3A–S3F; refs. 14, 35). All cell types were detected in both genotypes but differed in relative abundance (**Fig. 2D**; Supplementary Fig. S3E; Supplementary Table S2). Hypoxia and tissue dissociation signatures (36) remained low and comparable between genotypes, excluding stress-related artifacts (Supplementary Fig. S3G). ATM-deficient tumors contained increased malignant ductal and EMT-like cells, along with an altered stromal composition (**Fig. 2D**). AKPC tumors exhibited a myeloid-enriched profile, dominated by an accumulation of M1-like TAMs, whereas KPC tumors showed higher proportions of B and T lymphocytes in line with previous reports (Supplementary Fig. S3H and S3I; refs. 14, 43, 46, 47). Consistent with histology, AKPC tumors exhibited more fibroblasts overall, with an enrichment of αSMA^+ myCAFs expressing collagen and tenascin ECM genes (**Fig. 2D** and **E**; Supplementary Fig. S4A and S4B). In contrast, KPC tumors displayed increased iCAF and apCAF populations. Flow cytometry of dissociated tumors (gated consistently across genotypes using unstained controls) confirmed the enrichment of αSMA^+Ly6C^- myCAFs and the reduction of αSMA^-Ly6C^+ iCAFs in AKPC, resulting in an increased myCAF/iCAF ratio (**Fig. 2F**; Supplementary Fig. S4C). Interestingly, fibroblasts and CAFs from KPC and AKPC tumors also depicted distinct signaling profiles (**Fig. 2G** and **H**; Supplementary Fig. S4D). Both AKPC myCAF and iCAF subtypes upregulated genes involved in ECM organization, contractility, and TGFβ signaling, consistent with myofibroblastic programs. Single-cell trajectory analysis revealed distinct transitions among CAF subtypes in KPC tumors, whereas AKPC CAFs showed overlapping myCAF and iCAF states, suggesting enhanced myCAF differentiation dynamics (Supplementary Fig. S4E). No differences in chromatin accessibility or predicted TF activity were detected between KPC and AKPC CAFs, indicating that these programs were not driven by epigenetic remodeling (Supplementary Fig. S4F).

To investigate ATM-specific tumor–CAF interplay, we used a Transwell coculture system with tumor cells and PSCs as CAF precursors (29), enabling assessment of myCAF and iCAF traits (**Fig. 2I**; Supplementary Fig. S5A–S5D). ATM-deficient cancer cells (AKC or AKPC) induced αSMA^+ myCAF differentiation in PSCs independently of P53 status (**Fig. 2J**; Supplementary Fig. S5E and S5F). Conditioned medium-based experiments confirmed that ATM-null tumor secretomes drive myCAF reprogramming (Supplementary Fig. S5G and S5H). CAF marker analyses revealed distinct P53-dependent transcriptional programs driving myCAF differentiation (**Fig. 2J**; Supplementary Fig. S5E). In P53-deficient settings, ATM loss suppressed iCAF gene expression and upregulated myCAF markers (*ACTA2* and *POSTN*), whereas in P53-proficient tumors, it increased myCAF markers without affecting iCAF-associated genes. These findings were confirmed *in vivo*, with the increased expression of CTGF and POSTN and reduced CXCL2 and Ly6C in ATM-deficient tumors (Supplementary Fig. S5I).

We next employed the PUB scaffold model (33) to track CAF differentiation dynamics in a versatile and flexible coculture setting (Supplementary Fig. S5J). ATM-deficient grafts recapitulated *in vivo* tumor features, including spindle-shaped neoplastic epithelium and an activated myCAF-rich stroma, supporting their use for functional analyses. Finally, $ATM^{+/\Delta}$ human MIA PaCa-2 cells (8) and CRISPR-edited *ATM*-KO PDOs reproduced ATM-dependent myCAF programming in human PDAC systems (**Fig. 2K** and **L**; Supplementary Fig. S5K; Supplementary Table S3).

Global profiling of ATM-deficient tumor cells reveals actin cytoskeleton remodeling and a secretory program

After establishing that epithelial ATM loss of function promotes myCAF differentiation, we investigated the underlying tumor cell molecular programs using single-nucleus multiomics. EMT-like cells from AKPC tumors showed increased transcriptional programs for cell locomotion and invasion compared with KPC counterparts (**Fig. 3A** and **B**). Both malignant ductal and EMT-like populations also expressed higher levels of mesenchymal genes, corroborating that ATM loss is a driver of the mesenchymal phenotype, in line with the increased EMT-like cell proportion in AKPC tumors (**Fig. 2E** and **Fig. 3A–C**). Bulk RNA-seq on AKPC and KPC cell lines validated these findings, revealing downregulation of epithelial organization pathways (adherens junction, gap junction, and cell junction organization; **Fig. 3D** and **E**). Both single-cell and bulk transcriptomic analyses also demonstrated positive correlations between ATM deficiency and mitochondrial and respiratory programs (**Fig. 3B** and **E**). Conversely, ATM-proficient KPC cells exhibited upregulation of gene programs related to metabolism and immune regulation (**Fig. 3E**). Gene regulatory network inference further distinguished KPC and AKPC ductal cells. ATM-proficient cells showed higher predicted *Stat3*, *Stat5*, *Jun*, and *Nfkb2* TF activity with increased expression of inflammatory response and IL signaling targets, whereas AKPC ductal cells exhibited networks associated with cell stress response (Supplementary Fig. S6A and S6B). Proteomic profiling identified 208 proteins differentially regulated according to ATM status, capturing changes in cellular

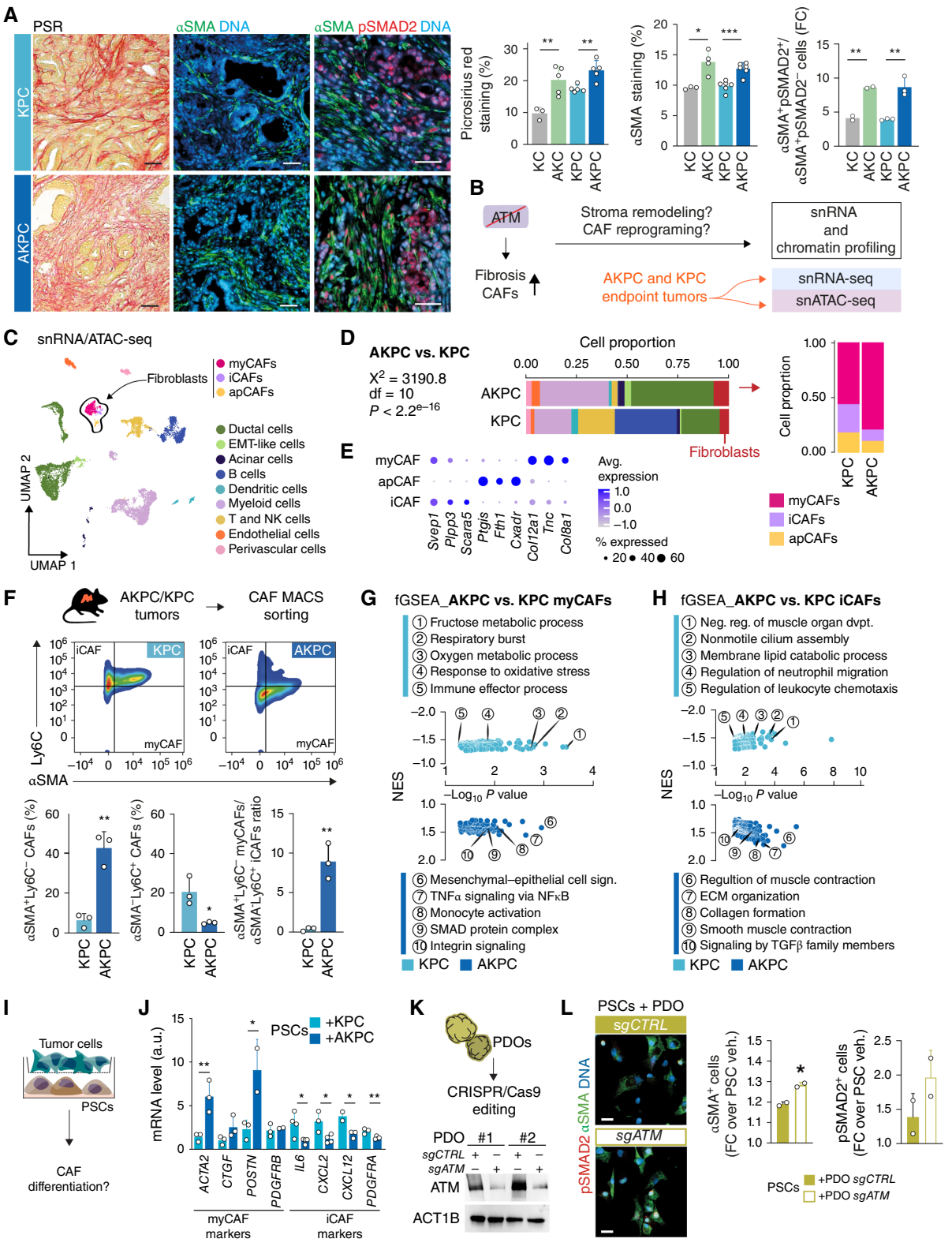


Figure 2.

ATM-deficient PDAC exhibits a myCAF-enriched stroma. **A,** Picrosirius red staining and immunofluorescence for αSMA and SMAD2 p-S465/S467 in endpoint KPC and AKPC tumors, with quantification of picrosirius red-positive, αSMA$^+$ surface, and αSMA$^+$SMAD2 p-S465/S467$^+$ cells vs. αSMA$^+$SMAD2 p-S465/S467$^-$ cells in endpoint KC, AKC (Supplementary Fig. S2A), KPC, and AKPC tumors. Nuclei were counterstained with DAPI. (*Continued on the following page.*)

Downloaded from http://aacrjournals.org/cancerres/article-pdf/doi/10.1158/0008-5472.CAN-26-0138/3803456/can-26-0138.pdf by DKFZ - German Cancer Research Center user on 25 June 2026

Downloaded from http://aacrjournals.org/cancerres/article-pdf/doi/10.1158/0008-5472.CAN-26-0138/3803456/can-26-0138.pdf by DKFZ - German Cancer Research Center user on 25 June 2026

organization, metabolism, and signaling pathways in AKPC cells. Corroborating the transcriptomic results, ATM loss positively correlated with enrichment in actin cytoskeleton organization and actomyosin machinery protein sets, suggesting enhanced contractility capacities (**Fig. 3D** and **F–H**; Supplementary Fig. S6C). Epithelial and EMT markers confirmed the mesenchymal phenotype associated with ATM deficiency (**Fig. 3C**; Supplementary Fig. S6D). ATM loss also correlated with enrichment in protein transport and exocytosis signaling, aligned with increased vesicle-mediated transport gene expression in AKPC ductal cells (**Fig. 3B** and **G**; Supplementary Fig. S6C). In contrast, ATM-proficient KPC cells showed protein expression patterns linked to epithelial differentiation and prominent immune tropism (**Fig. 3H**; Supplementary Fig. S6C).

Altogether, these data underpin that ATM loss of function in PDAC cells not only drives mesenchymal programming but also alters secretory phenotypes, whereas ATM-proficient cells retain epithelial differentiation and an immunoregulatory phenotype, suggesting distinct dialogs with their respective TME (**Fig. 3I**).

Stromal myCAF programming driven by the ATM-null tumor epithelium is TGFβ-dependent

To identify factors mediating ATM-specific tumor–stroma interplay, including low-abundant secreted molecules poorly detected by shotgun mass spectrometry, we analyzed tumor cell secretomes using a targeted antibody microarray approach (**Fig. 4A**; ref. 48). AKPC secretomes showed enrichment of inflammatory cytokines and chemokines, integrins, and growth factors linked to actin cross-linking, actin cytoskeleton, and chemotaxis (**Fig. 4B** and **C**).

Among proteins enriched in ATM-null secretomes, TGFβ1 emerged as a candidate regulator given its established role in myCAF differentiation (21). In contrast, KPC secretomes were enriched in proteins involved in B-cell regulation and ECM-binding pathways, consistent with an inflammatory phenotype (Supplementary Fig. S7A). The iCAF inducer IL1α (21) was detected in both AKPC and KPC secretomes, suggesting spatial coexistence or dynamic plasticity of CAF subtypes within the TME (**Fig. 4B** and **D**). ATM-dependent TGFβ1 regulation seemed posttranslational, as mRNA levels remained unchanged, whereas protein release increased in ATM-deficient mouse cancer lines and ATM-KO human hPANC lines (**Fig. 4E** and **F**; Supplementary Fig. S7B and S7C). Consistently, no differences in TGFβ ligands mRNA or protein levels were detected between KPC and AKPC ductal and EMT-like cells (Supplementary Fig. S7D and S7E). myCAFs expressed the highest levels of TGFβ receptors, underscoring their role as primary TGFβ-responsive cells independent of epithelial genotype. Although receptor gene expression varied between KPC and AKPC malignant cells, protein abundances were comparable (Supplementary Fig. S7E and S7F). Secretomes of ATM-deficient cells demonstrated greater activation of a TGFβ-responsive reporter compared with ATM-proficient cells (Supplementary Fig. S7G). Consistently, TGFβ1 accumulated in the ATM-deficient TME, colocalizing with αSMA^+ and $pSMAD2^+$ stromal regions (**Fig. 4G**; Supplementary Fig. S7H).

To determine whether this effect depended on ATM kinase activity, ATM-wild-type KC and KPC cells were treated with a clinical-grade ATM inhibitor. ATM kinase inhibition increased TGFβ signaling activity of conditioned media from ATM-proficient cells, suggesting a direct role of ATM in regulating TGFβ1 bioavailability (**Fig. 4H**). CellChat analysis further revealed distinct tumor–stroma communication patterns between KPC and AKPC tumors (Supplementary Fig. S7I). TGFβ signaling mediated interactions between EMT-like cells and CAFs in ATM-deficient tumors, whereas it was primarily involved in macrophage-CAF cross-talk in KPC tumors (**Fig. 4I**). Ligand–receptor analysis identified multiple TGFβ superfamily members (e.g., *Tgfb2*, *Tgfbr1*, and *Acvr1*) and integrins regulating TGFβ bioavailability (e.g., *Itgav* and *Itgb1*; ref. 50) specifically in AKPC tumors (**Fig. 4J**; Supplementary Fig. S7J). CAF populations in AKPC tumors displayed more active TGFβ-responsive transcriptional programs (49), indicating a feed-forward signaling loop driven by epithelial ATM loss (**Fig. 4K**; Supplementary Fig. S7K). Genes encoding TGFβ activators (e.g., integrins and *Thbs1*) also showed a trend toward increased expression in CAFs and malignant cells in the ATM-deficient context (Supplementary Fig. S7L and S7M).

To test causality between ATM deficiency, TGFβ signaling, and myCAF differentiation, AKC, AKPC, and ATM-KO hPANC tumor cell–PSC cocultures were treated with the TGFBR1 inhibitor SB431542 (TβRi), which blocks canonical TGFβ signaling. TβRi suppressed myCAF programming, confirming the direct involvement of the TGFβ/SMAD axis (**Fig. 4L** and **M**; Supplementary Fig. S7N–S7P). Conversely, iCAF marker expression increased upon TβRi, further illustrating the CAF fate switch. Similar results were obtained using the *ex vivo* PUB assay (Supplementary Fig. S7Q).

Because BMP signaling has been implicated in ATM-deficient tumors (24), we examined its contribution to CAF reprogramming and interaction with TGFβ signaling. However, multiomics analysis revealed no enrichment of the BMP4-responsive signature between AKPC and KPC tumors (Supplementary Fig. S8A and S8B). Although recombinant BMP4 induced myCAF traits in PSCs, BMP pathway inhibition in PSC-ATM-deficient tumor cell cocultures did not suppress myCAF programming and only modestly increased iCAF markers (Supplementary Fig. S8C and S8D). In contrast, cocultures with CRISPR-edited TGFB1-KO AKC and AKPC tumor cells confirmed tumor-derived TGFβ1 as the central driver of myCAF programming in the ATM-null setting (**Fig. 4N**; Supplementary Fig. S8E and S8F).

Given that CAFs can arise from multiple precursor populations, we explored CAF ontogeny using PSC- and non–PSC-derived signatures

(*Continued*.) Scale bars, 100 μm. Mean ± SD of ≥3 KPC and AKPC and ≥2 KC and AKC mice; each dot represents a mouse. **B,** Single-cell multiomic workflow (snRNA/snATAC) of KPC ($n = 2$) and AKPC ($n = 2$) tumors. **C,** UMAP of integrated snRNA-seq/snATAC-seq data showing cell clusters in KPC and AKPC tumors. **D,** Proportion of cells from KPC and AKPC tumors and distribution of myCAF, iCAF, and apCAF subpopulations within fibroblasts. **E,** Dot plot of the top three genes defining myCAF, iCAF, and apCAF subpopulations. **F,** Representative flow cytometric analysis and quantification of αSMA^+Ly6C^- and αSMA^-Ly6C^+ CAFs in endpoint KPC and AKPC tumors. Mean ± SD of three KPC and AKPC mice; each dot represents a mouse; unpaired Student *t* test. **G** and **H,** GSEA (GO, REACTOME, and hallmark) showing pathways upregulated and downregulated ($P < 0.05$) in AKPC vs. KPC myCAFs (**G**) and iCAFs (**H**). **I,** Schematic of the transwell coculture assay. **J,** qPCR of myCAF and iCAF markers in PSCs cocultured for 72 hours with KPC or AKPC tumor cells. Mean ± SD of ≥2 cell lines/genotype (tested in ≥2 independent experiments); each dot represents a cell line. **K,** Immunoblot for ATM in *sgATM* or *sgCTRL* PDOs. **L,** Immunofluorescence for αSMA and SMAD2 p-S465/S467 with quantification of αSMA^+ and SMAD2 p-S465/S467$^+$ PSCs vs. inactivated PSCs after 72 hours of coculture with *sgATM* or *sgCTRL* PDOs as in **I**. Mean ± SD of two PDO lines (tested in three independent experiments); each dot represents a cell line. **A, J,** and **L,** Unpaired Student *t* test. *, $P < 0.05$; **, $P < 0.01$; ***, $P < 0.001$. NES, normalized enrichment scale.

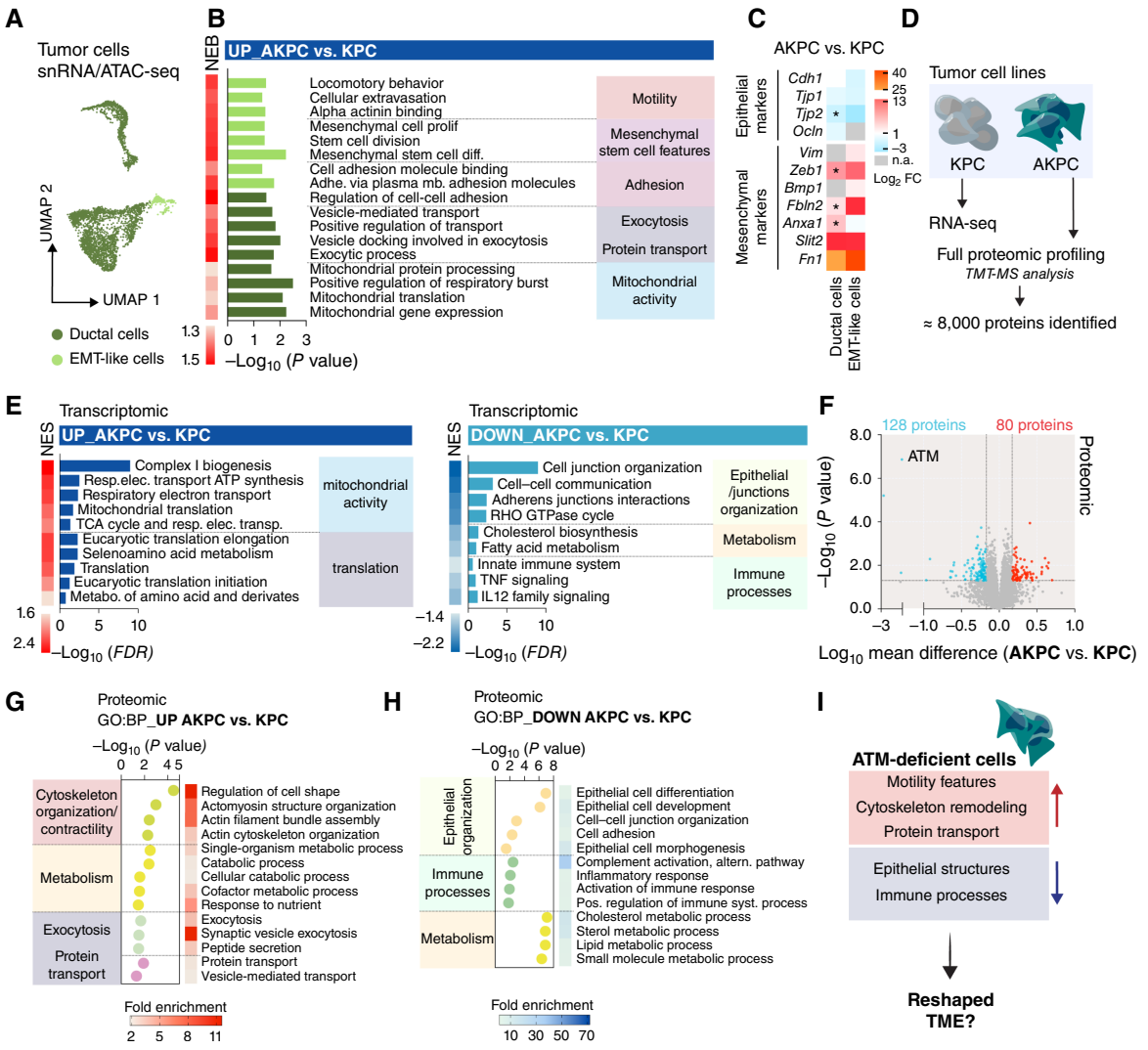


Figure 3.

Transcriptomic and proteomic profiling of ATM-deficient tumor cells reveals an actin cytoskeleton remodeling and secretory program. **A** and **B,** UMAP of integrated snRNA-seq/ATAC-seq data from KPC and AKPC tumors showing EMT-like and ductal populations (**A**), and GSEA (GO, REACTOME, and hallmark) showing pathways upregulated in AKPC vs. KPC EMT-like and ductal cells (P <0.05; **B**). **C,** Heatmap of epithelial and mesenchymal gene expression in AKPC vs. KPC ductal and EMT-like cells. **D,** Schematic of the transcriptomic and proteomic approaches in KPC and AKPC cell lines. **E,** GSEA (REACTOME and KEGG) showing pathways downregulated and upregulated in AKPC (n = 4) vs. KPC (n = 5) cell lines (FDR <0.05). **F,** Volcano plot displaying differential protein abundance between AKPC (n = 5) and KPC (n = 5) cells (P <0.05; fold change ≥1.5). **G** and **H,** GO:BP annotations for proteins upregulated (**G**) and downregulated (**H**) in AKPC vs. KPC cells (P <0.05). **I,** Schematic illustrating the main phenotypic features of KPC and AKPC cells. *, P <0.05. NES, normalized enrichment scale.

(51). myCAF and iCAF clusters were enriched for a non-PSC signature, whereas apCAFs more frequently showed PSC-derived profiles irrespective of tumor genotype (Supplementary Fig. S8G). To extend findings beyond PSC-derived models, we conducted coculture experiments with CAFs derived from two independent mouse models. ATM-deficient tumor cells similarly induced myCAF reprogramming, although marker patterns differed between PSCs and primary CAFs (**Fig. 4O**; Supplementary Fig. S8H-S8J). These results suggest that myCAF differentiation is not restricted by precursor origin, though cellular identity may shape transcriptional programs.

Finally, *in vivo* subcutaneous coculture experiments with tumor cells and PSCs were performed using the clinical TGFBR1 inhibitor galunisertib (**Fig. 4P**; ref. 52). ATM-deficient tumors exhibited marked αSMA$^+$ myCAF enrichment. TGFβ interference showed no effect on αSMA levels in ATM-proficient KPC tumors but significantly reduced αSMA$^+$ stroma in AKPC specimen. The KRAS^{G12D} inhibitor MRTX1133, which promotes myCAF accumulation (53), increased αSMA$^+$ fibroblasts in both genotypes (**Fig. 4P**; Supplementary Fig. S8K). In contrast, TGFβ inhibition specifically reshaped myCAFs in ATM-deficient tumors, connecting epithelial ATM status to stromal reprogramming independently of KRAS signaling (Supplementary Fig. S8K).

Together, these data highlight an ATM loss-dependent TGFβ signaling axis between malignant cells and CAFs that promotes a

Downloaded from http://aacrjournals.org/cancerres/article-pdf/doi/10.1158/0008-5472.CAN-26-0138/3803456/can-26-0138.pdf by DKFZ - German Cancer Research Center user on 25 June 2026

myCAF-enriched microenvironment through posttranslational regulation of TGFβ activity, distinct from the inflammatory phenotype observed in ATM-proficient tumors.

A deregulated actomyosin network in ATM-deficient PDAC cells supports TGFβ-induced myCAF differentiation

TGFβ bioavailability has been reported to depend on integrin expression patterns intimately linked to actin cytoskeleton dynamics and contractile force (54). Consistent with our *in vivo*, *in vitro*, transcriptomic, and proteomic data indicating more adhesive and contractile properties upon ATM deletion, ACTN4, a critical actin cross-linker of the actomyosin machinery, was upregulated in the ATM-null background (**Fig. 5A–C**; Supplementary Fig. S9A and S9B). PXN and VINC, proteins involved in focal adhesion dynamics, cytoskeleton rearrangement, and cell contractility regulation, were similarly increased. ATM-KO hPANC cells recapitulated this contractile phenotype in a human PDAC model (**Fig. 5D**). To further characterize this phenotype, we assessed the ability of ATM-deficient cells to progress through confined microchannels designed to measure contractility-dependent single-cell migration, a feature predictive of metastatic potential (32). Following our previous results, AKPC cells showed enhanced migration through microchannels, attesting to high cellular plasticity and contractile capacity (**Fig. 5E**). ATM-deficient AKPC cells were also enriched for mitochondrial activity and oxidative phosphorylation gene sets, suggesting dysregulated ROS production (**Fig. 3B** and **E**; Supplementary Fig. S9C). Accordingly, AKPC, AKC, and ATM-KO hPANC cells exhibited higher ROS levels than their ATM-proficient counterparts (**Fig. 5F**; Supplementary Fig. S9D). ATM inhibition similarly induced ROS accumulation and promoted a contractile phenotype (Supplementary Fig. S9E–S9G). ROS production is accentuated under oncogenic stress, including DNA damage accumulation (55), and has been proposed to affect cellular contractility (56). To determine whether ROS drive the contractile and secretory phenotype of ATM-deficient PDAC cells and promote myCAF programming, we performed loss-of-function experiments targeting ROS production and contractility regulators (**Fig. 5G**). CRISPR-mediated KO of *Keap1*, the main intracellular inhibitor of NRF2 (57), enhanced antioxidant activity and markedly reduced ROS levels in AKPC and AKC tumor cells (**Fig. 5H**). KEAP1-deficient cells displayed improved epithelial organization, reduced ACTN4 and PXN expression, and decreased motility, resembling the phenotype observed in PXN- or ACTN4-KO AKC and AKPC cells (**Fig. 5I** and **J**). Additionally, mitochondrial ROS inhibition with YCG063 further validated the ROS-contractility axis (Supplementary Fig. S9H–S9L). Conversely, ROS induction using the oxidant menadione increased ACTN4 and PXN expression in AKPC cells, supporting a functional link between ROS overproduction and tumor cell contractility (Supplementary Fig. S9M and S9N).

Finally, we asked whether ROS-driven contractility in ATM-deficient tumor cells regulates TGFβ1 secretion and CAF differentiation. Loss of ACTN4 or PXN produced modest, nonsignificant reductions in TGFβ1 secretion and partially attenuated myCAF induction, consistent with the functional redundancy of actin–myosin and focal adhesion networks (e.g., ACTN paralogs and PXN–VINC–TLN modules; ref. 58). In contrast, KEAP1 KO robustly decreased TGFβ1 secretion and impaired PSC-to-myCAF differentiation (**Fig. 5K** and **L**), placing ROS upstream of both contractility and TGFβ1 bioavailability in ATM-deficient PDAC cells. Consistently, coculture and conditioned-medium experiments showed reduced canonical TGFβ signaling and diminished αSMA$^+$ myCAF differentiation (**Fig. 5L**; Supplementary Fig. S9O-S9R). Thus, we propose that ATM deficiency initiates a cascade in which genomic instability leads to ROS accumulation, thereby driving aberrant actomyosin contractility and secretory remodeling, which elevate TGFβ1 bioavailability and ultimately reprogram the TME toward a myCAF-enriched state.

The myCAF-enriched TME in ATM-deficient PDAC drives chemoresistance and invasiveness

HRD confers sensitivity to platinum-based regimens such as FOLFIRINOX (3, 5, 7), yet a substantial proportion of HR-deficient cancers fail to respond (59). To test whether ATM-dependent niche reprogramming mediates chemoresistance, we evaluated oxaliplatin response. Despite comparable cytotoxic effects across genotypes, PSCs conferred resistance selectively in ATM-deficient cells, implicating the TGFβ-driven myCAF programming (**Fig. 6A**; Supplementary Fig. S10A). To assess the efficacy of combined TGFβ interference and FOLFIRINOX, we employed the PUB system as an *ex vivo* drug-testing platform. Consistent with their HRD, only ATM-null tumor cells responded to the platinum-based FOLFIRINOX regimen. TGFβ pathway inhibition further enhanced FOLFIRINOX cytotoxicity selectively in ATM-depleted cells. Notably, TGFβ inhibition alone caused cytotoxic effects in ATM-deficient cancer cells, indicating partial cell-autonomous dependence (**Fig. 6B**; Supplementary Fig. S10B).

Given reports that stromal or DDR-targeted therapies can promote aggressive tumor phenotypes (7, 8, 16, 60), we asked whether combined FOLFIRINOX and TGFβ inhibition induces invasive selection. In the PUB system, ATM-deficient tumor cells exhibited the highest capacity for ECM infiltration, which was diminished by TGFβ inhibition (Supplementary Fig. S10C–S10E), arguing against the selection of more invasive clones. Consistently, TGFβ1 ablation reduced AKC and AKPC tumor cell motility without increasing sensitivity to FOLFIRINOX components (Supplementary Fig. S10F–S10I), suggesting that although tumor-derived TGFβ1 directly regulates migration, it mediates chemoresistance indirectly through TGFβ-dependent myCAF programming.

Upon orthotopic transplantation, AKC and AKPC tumor cells formed PDACs with dense αSMA$^+$ myCAF–enriched stroma, which was reversed by galunisertib (**Fig. 6C** and **D**; Supplementary Fig. S11A–S11C). FOLFIRINOX or galunisertib alone prolonged survival exclusively in ATM-null tumor-bearing mice (**Fig. 6E**; Supplementary Fig. S11D). Their combination further improved survival and reduced fibrosis, consistent with longitudinal imaging (**Fig. 6D** and **E**; Supplementary Fig. S11A–S11E). This therapeutic benefit was associated with decreased proliferation and increased apoptosis selectively in ATM-null genotypes and was notably attenuated in the absence of P53 (**Fig. 6E**; Supplementary Fig. S11F–S11H).

Given evidence that myCAF targeting can be counteracted by compensatory iCAF expansion (21), we examined CAF plasticity following TGFβ signaling inhibition. Although galunisertib had minimal effect on PDPN$^+$Ly6C$^+$ iCAFs in KC and KPC tumors, ATM-deficient AKC and AKPC tumors exhibited significant iCAF accumulation, reflected by increased PDPN$^+$pSTAT3$^+$ cells and a decreased αSMA$^+$ myCAF/Ly6C$^+$ iCAF ratio (**Fig. 6F**; Supplementary Fig. S11I and S11J). These findings suggest a CAF phenotypic shift that may undermine therapeutic efficacy through iCAF-driven signaling.

To evaluate translational relevance, we used two human-derived preclinical orthotopic models based on hPANC cells and PDOs and observed genotype-specific efficacy of combined TGFβ inhibition

Downloaded from http://aacrjournals.org/cancerres/article-pdf/doi/10.1158/0008-5472.CAN-26-0138/3803456/can-26-0138.pdf by DKFZ - German Cancer Research Center user on 25 June 2026

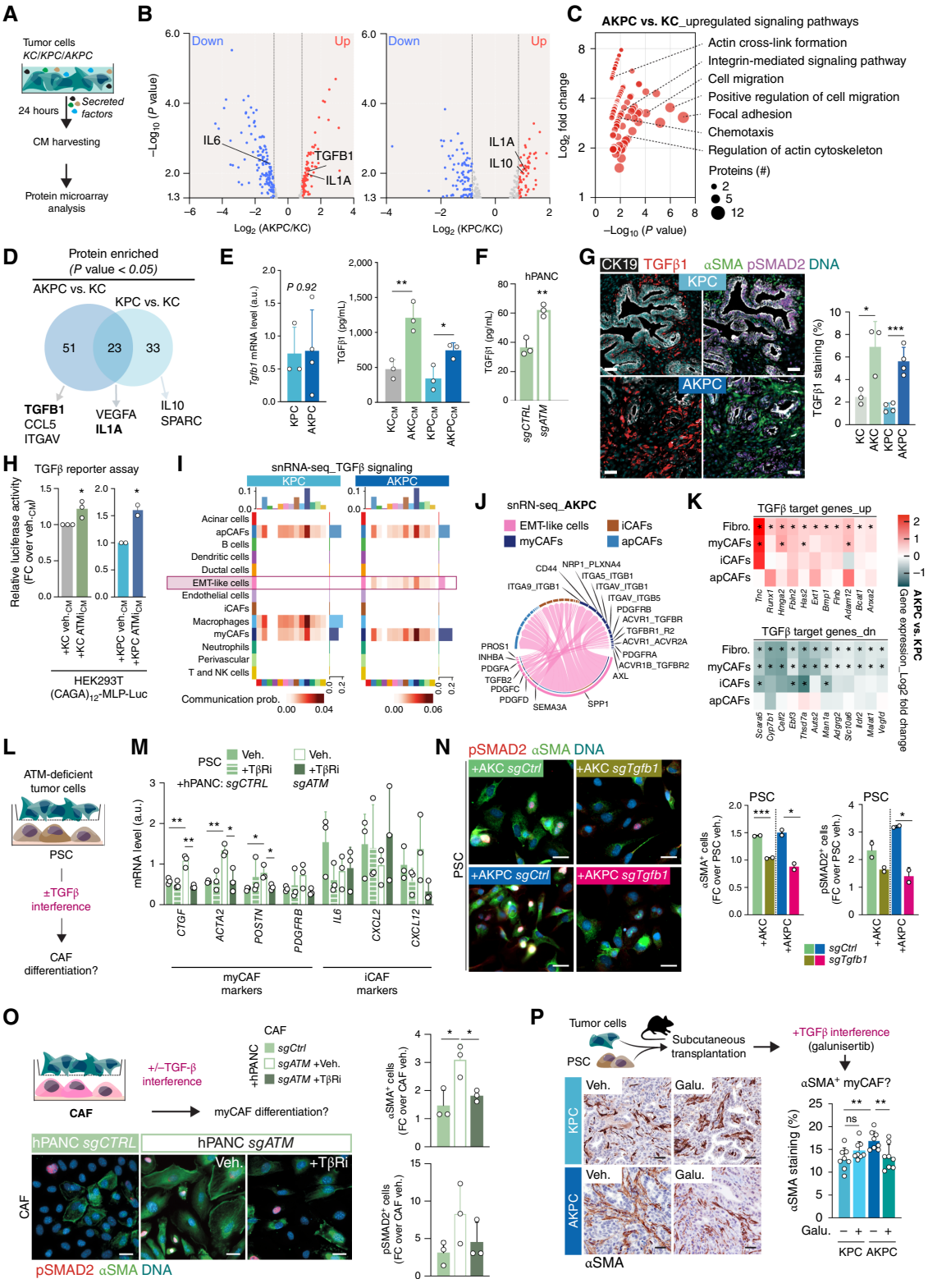


Figure 4.

TGFβ1 released by ATM-deficient tumor cells drives myCAF differentiation. **A,** Secretome profiling workflow in KC ($n = 3$), KPC ($n = 3$), and AKPC ($n = 2$) cell lines. **B,** Differential protein abundance in AKPC vs. KC and KPC vs. KC secretomes. Red and blue dots indicate upregulated and downregulated proteins (P <0.05; fold change ≥1.8) in AKPC ($n = 2$) and KPC ($n = 3$) vs. KC ($n = 3$) cell lines. **C,** KEGG, BioCarta, and GO:BP (*Continued on the following page.*)

Downloaded from http://aacrjournals.org/cancerres/article-pdf/doi/10.1158/0008-5472.CAN-26-0138/3803456/can-26-0138.pdf by DKFZ - German Cancer Research Center user on 25 June 2026

and FOLFIRINOX in ATM-deficient PDAC (**Fig. 6G–I**). Therapeutic effects exceeded those in mouse-derived models, with five of six ATM-KO hPANC and three of four ATM-KO PDO–transplanted mice reaching the experimental endpoint under combination treatment. This benefit correlated with marked TME remodeling, including reduced myCAF accumulation and fibrosis (**Fig. 6J**).

ATM-deficient human pancreatic cancers exhibit distinct TME features

To assess whether ATM-specific stromal alterations extend to human PDAC, we performed transcriptomic deconvolution of the TCGA-PAAD bulk RNA-seq data (61) using BayesPrism (**Fig. 7A**; Supplementary Fig. S12A and S12B; ref. 41). Deconvolution using scRNA-seq references from two independent studies (14, 42) identified major cell populations, including malignant and healthy ductal cells and fibroblast subsets (myCAFs, iCAFs, and non-CAFs). Accuracy was supported by a strong correlation between inferred pseudobulk and reference profiles. Given the low incidence of ATM mutations, tumors were stratified by *ATM* expression levels as a surrogate for functional status (Supplementary Fig. S12C; ref. 24). *ATM* expression negatively correlated with malignant ductal cell abundance and positively with healthy ductal cells, supporting an association between low *ATM* levels and malignant expansion (**Fig. 7A**). We next examined whether epithelial *ATM* expression relates to CAF composition. *ATM* expression in malignant ductal cells inversely correlated with myCAF abundance and positively with iCAF proportions, recapitulating the CAF programming observed in ATM-deficient AKC and AKPC models (**Fig. 7B**). Extending this analysis to other DDR genes, expression-based stratification revealed that *ATM*, *RAD51C*, and *FANCG* uniquely exhibited negative correlations with the myCAF/iCAF ratio, whereas *ATR*, *PALB2*, and *BRCA1* showed positive associations (**Fig. 7C** and **D**; Supplementary Fig. S12C), as previously reported (62). In parallel, reduced *ATM* and *FANCG* expression, but not *BRCA1* and *ATR*, was associated with ROS signature enrichment (**Fig. 7E**), consistent with the ROS–myCAF axis identified above. These findings support a tumor-intrinsic role for ATM loss in driving myCAF-enriched stromal remodeling and highlight nonredundant functions of specific DDR components in shaping the PDAC TME.

To validate these findings, we analyzed a clinically annotated cohort of *ATM*-mutated human PDACs (Supplementary Table S4). As *ATM* pathogenic mutations are predominantly truncating, resulting in unstable protein products, and are largely mutually exclusive with *TP53* mutations (Supplementary Fig. S12C; ref. 63), analyses focused on *ATM*-mutant, *TP53*-wild-type tumors to assess the impact of epithelial ATM loss of function on CAF fate. IHC showed a trend toward increased myCAF-associated αSMA in the peritumoral stroma of *ATM*-mutated PDAC compared with *ATM*-wild-type tumors (**Fig. 7F**). We next examined *BRCA1*-and *ATR*-mutated PDAC models to determine whether these stromal features extend beyond ATM-deficient PDAC. *BRCA1*-mutant cancers instead displayed a predominantly αSMA^{low} CAF profile, contrasting with the αSMA-enriched phenotype observed in *ATM*-mutant PDAC (**Fig. 7G**). To functionally assess DDR gene specificity, ATR deficiency was modeled by CRISPR-mediated KO in KC cells. ATR loss failed to recapitulate the ROS–TGFβ–myCAF axis observed upon ATM loss, despite functional overlap with ATM in HR repair (Supplementary Fig. S12D–S12G). Consistently, *ATR*-mutant patient-derived xenograft models showed no added benefit from combined FOLFIRINOX and TGFβ inhibition compared with chemotherapy alone (Supplementary Fig. S12H).

Together, these human data underscore the pivotal role of ATM loss of function and broader epithelial HRD status in orchestrating TME programming, as evidenced by the myCAF-enriched pattern and heightened ROS stress in ATM-deficient PDAC (**Fig. 7H** and **I**).

Discussion

A one-size-fits-all approach to PDAC is unattainable. Current stratification focuses on epithelial genetics and offers limited therapeutic guidance. Most additional classifiers are prognostic and noninstructive. Targeting intratumoral communication between the epithelium and niche may add a therapeutic layer. Prior trials targeting cancer-TME signaling (e.g., Hedgehog) failed, likely due to nonselective, nongenotype-stratified stroma depletion (16, 18). CAF heterogeneity, with tumor-promoting and tumor-restraining PDAC subsets, remains a major constraint (64). The mechanisms driving this heterogeneity remain largely unexplored, hampering genotype-tailored stromal interventions.

(*Continued.*) enrichment analyses of proteins enriched in AKPC vs. KC secretomes. **D,** Venn diagram showing overlap of enriched proteins between AKPC and KPC secretomes. **E,** qPCR of *Tgfb1* in KPC and AKPC tumor cells and ELISA for TGFβ1 in conditioned medium (CM) from KC, AKC, KPC, and AKPC cells. Mean ± SD of ≥3 cell lines/genotype (tested in ≥2 independent experiments) for qPCR; ≥2 CM batches/cell line were tested for ELISA. Each dot represents a cell line. **F,** ELISA for TGFβ1 in CM from *sgATM* and *sgCTRL* hPANC cells. Each dot represents a cell line, with ≥2 CM batches/cell line. **G,** Immunofluorescence for CK19/TGFβ1 and αSMA/SMAD2 p-S465/S467 with quantification of $TGF\beta1^+$ surface in endpoint KC, AKC (Supplementary Fig. S7H), KPC, and AKPC tumors. Nuclei were counterstained with DAPI. Scale bars, 100 μm. Mean ± SD (4 KPC and AKPC; 3 KC and AKC mice); each dot represents a mouse. **H,** SMAD-responsive $(CAGA)_{12}$-Luc reporter activity in HEK293T cells treated for 48 hours with CM from KC and KPC cells treated or not with the ATM inhibitor AZD0156 (1 μmol/L). Mean ± SD of ≥2 cell lines/genotype (≥2 CM batches/cell line were tested); each dot represents a cell line. **I** and **J,** Inferred communication probability via TGFβ signaling between cell clusters in KPC and AKPC tumors (**I**) and inferred ligand–receptor interactions between EMT-like cells and CAF subpopulations in AKPC tumors (**J**). **K,** Heatmap of TGFβ target genes upregulated or downregulated in fibroblasts (49) in AKPC vs. KPC fibroblasts, myCAFs, iCAFs, and apCAFs. Stars indicate adjusted $P < 0.05$. **L,** Schematic of the transwell coculture assay. **M,** qPCR of myCAF and iCAF markers in PSCs cocultured for 72 hours with *sgATM* or *sgCTRL* hPANC cells and treated or not with the TGFBR1 inhibitor SB431542 (TβRi; 10 μmol/L). Mean ± SD of three cell lines/genotype (tested in ≥2 independent experiments); each dot represents a cell line. **N,** Immunofluorescence for αSMA and SMAD2 p-S465/S467 on PSCs cocultured for 72 hours with *sgTgfb1* or *sgCTRL* AKC or AKPC cells and quantification of αSMA^+ and SMAD2 p-S465/S467$^+$ PSCs. Nuclei were counterstained with DAPI. Scale bars, 20 μm. Mean ± SD of two cell lines/genotypes (tested in three independent experiments); each dot represents a cell line. **O,** Schematic of the transwell coculture assay and immunofluorescence for αSMA and SMAD2 p-S465/S467 in CAF lines cocultured for 72 hours with *sgAtm* or *sgCTRL* hPANC cells, with quantification of αSMA^+ and SMAD2 p-S465/S467$^+$ CAFs. Nuclei were counterstained with DAPI. Scale bars, 20 μm. Mean ± SD of three cell lines/genotypes (tested in two independent experiments); each dot represents a cell line. **P,** Subcutaneous assay and αSMA IHC with quantification of αSMA^+ staining in tumors from KPC or AKPC cells cotransplanted with PSCs and treated or not with galunisertib (galu.). Scale bars, 50 μm. Mean ± SD; each dot represents a subcutaneous tumor. **E–H, M,** and **N–P,** unpaired Student *t* test. *, $P < 0.05$; **, $P < 0.01$; ***, $P < 0.001$.

Downloaded from http://aacrjournals.org/cancerres/article-pdf/doi/10.1158/0008-5472.CAN-26-0138/3803456/can-26-0138.pdf by DKFZ - German Cancer Research Center user on 25 June 2026

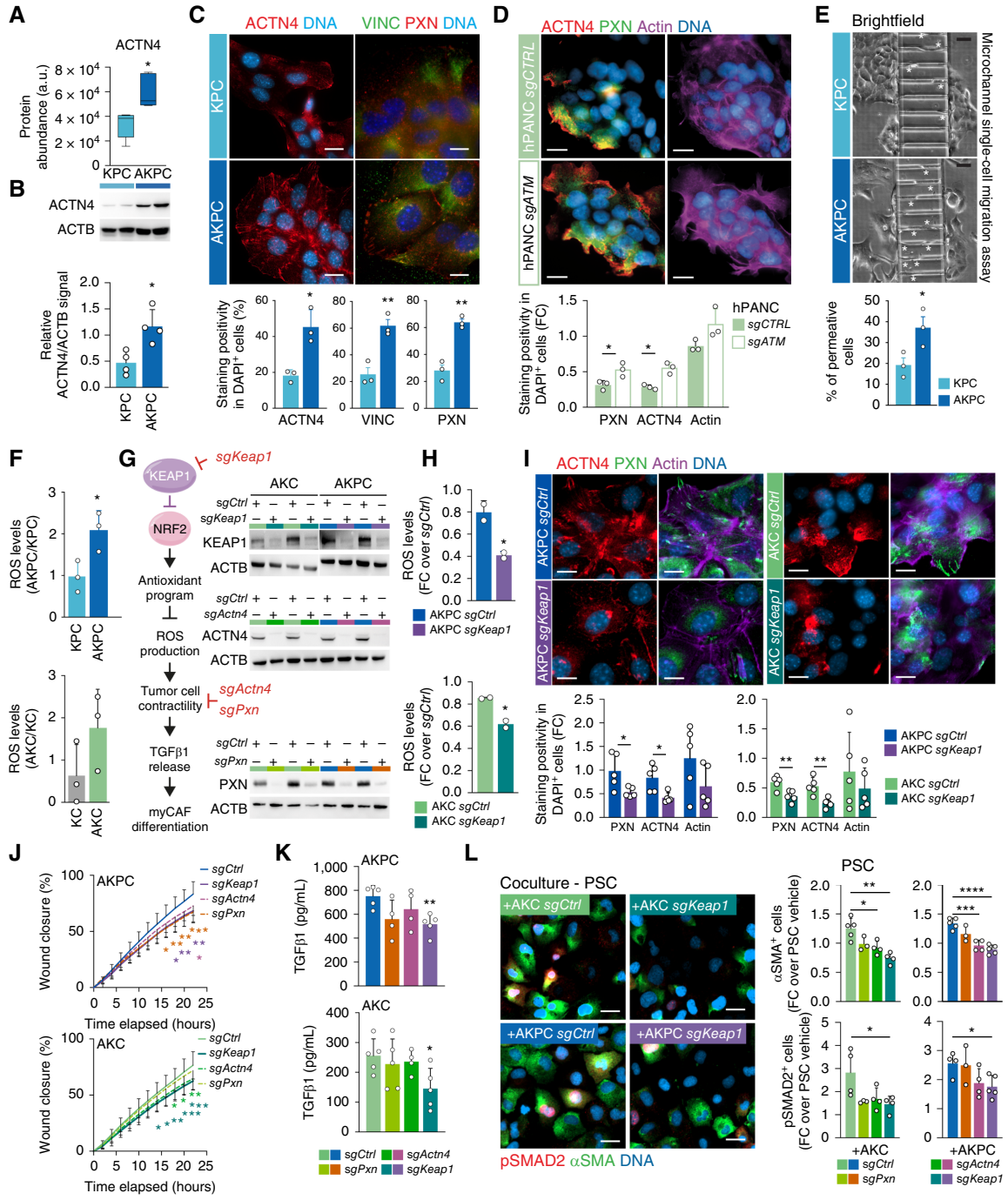


Figure 5.

A deregulated actomyosin network in ATM-deficient PDAC cells supports TGFβ-induced myCAF differentiation. **A,** ACTN4 protein abundance in KPC ($n = 5$) and AKPC ($n = 5$) cell lines. **B,** Immunoblot and quantification of ACTN4 in KPC and AKPC tumor cells. Mean ± SD of four independent experiments (2 cell lines/genotype), each dot represents an experiment. **C,** Immunofluorescence for ACTN4, VINC, and PXN on KPC and AKPC tumor cells with quantification of ACTN4$^+$, VINC$^+$, and PXN$^+$ staining in DAPI$^+$ cells. Nuclei were counterstained with DAPI. Scale bars, 20 μm. Mean ± SD of three independent experiments (≥2 cell lines/genotype), each dot represents an experiment. **D,** Immunofluorescence for ACTN4 and PXN and phalloidin-Atto565 staining (cortical F-actin) in *sgATM* and *sgCTRL* hPANC cells with quantification of ACTN4$^+$, PXN$^+$, and F-actin$^+$ staining in DAPI$^+$ cells. Nuclei were counterstained with DAPI. Scale bars, 20 μm. Mean ± SD of 3 cell lines/genotype (tested in two independent experiments); each dot represents a cell line. **E,** Microchannel single-cell migration assay with proportions of permeative cells. Asterisks show migrating cells. Scale bars, 50 μm. Mean ± SD of four independent experiments (3 cell lines/genotype), each dot represents an experiment. **F,** ROS levels in KPC and AKPC, KC, and AKC cells. Mean ± SD of 3 cell lines/genotype (tested in ≥2 independent experiments); each dot represents a cell line. **G,** Schematic of the proposed ROS-mediated cascade driving myCAF differentiation in ATM-deficient tumors, with CRISPR/Cas9-targeted genes in red, and immunoblot for KEAP1, ACTN4, and PXN in *sgKeap1*, *sgActn4*, *sgPxn*, or *sgCtrl* AKC and AKPC cells. (*Continued on the following page.*)

Downloaded from http://aacrjournals.org/cancerres/article-pdf/doi/10.1158/0008-5472.CAN-26-0138/3803456/can-26-0138.pdf by DKFZ - German Cancer Research Center user on 25 June 2026

Downloaded from http://aacrjournals.org/cancerres/article-pdf/doi/10.1158/0008-5472.CAN-26-0138/3803456/can-26-0138.pdf by DKFZ - German Cancer Research Center user on 25 June 2026

We show that ATM loss not only promotes epithelial-intrinsic aggressiveness but also triggers TGFβ release via a ROS–actomyosin–contractility axis. TGFβ1 drives myCAF enrichment in mouse and human cancers, reinforcing mesenchymal phenotypes, aggressiveness, and ECM deposition (24). Disrupting this cross-talk with TGFβ inhibitors plus chemotherapy exposes a druggable vulnerability of ATM-deficient and potentially other HRD PDAC. ACTN4 and PXN KOs had modest effects on TGFβ1 secretion and myCAF induction, reflecting the redundancy within actin–myosin and focal adhesion networks (58, 65). In contrast, KEAP1 inactivation reduced ROS and suppressed myCAF programming, indicating ROS dependence of contractility and TGFβ1 availability. ROS also promotes mesenchymal phenotypes (66). In ATM-deficient cells, ROS may therefore alter epithelial identity directly and, in parallel, increase TGFβ1 secretion and tumor cell–intrinsic signaling.

ATM-null PDAC displays HRD-driven genomic instability due to impaired DSB repair (5, 6). AKC cells upregulate P53, suggesting a compensatory activation that may restrain ATM loss-of-function consequences during pancreatic carcinogenesis. ATM/P53 codeletion yields highly invasive PDAC, surpassing P53 loss alone, stressing the existence of independent roles for ATM and P53. The stromal programming axis identified here operates independently of P53 loss of function, extending its relevance. P53 alterations differentially educate CAFs (67). ATM loss instead reshapes myCAF identity and dominates over P53 status, indicating a hierarchical effect on stromal traits. As a limitation, endpoint-derived cell lines have undergone selection for clones that bypass p53/ATM pathway antagonism, which can limit the capture of early genotype-dependent vulnerabilities.

Of note, although ATM loss reproducibly activated the ROS–TGFβ–myCAF program, BRCA1-or ATR-mutant PDACs instead displayed immunoregulatory CAF enrichment (62). This divergence suggests distinct genotype-specific TME states that may be exploitable as personalized add-on therapies in combination with the standard of care.

BMP4/SMAD1 signaling is part of the rewired TGFβ superfamily in ATM-deficient pancreas and is linked to EMT (24). Here, ATM deficiency in adenocarcinoma primarily activates a ROS–TGFβ axis driving myCAF programming. The modest BMP4 contribution suggests context dependence across genotype, stage, and compartment. We propose a unified model in which ATM loss engages multiple TGFβ superfamily branches: BMP/activin dominates early to remodel the epithelium, whereas in advanced PDAC, contractility-driven TGFβ release reprograms the TME.

TGFβ bioavailability is regulated by multiple mechanisms, including integrin-mediated activation (50), which converts cytoskeletal tension into mechanical forces on the latent TGFβ complex to release the active cytokine. ATM loss promotes a contractile and migratory phenotype consistent with EMT (24), with increased expression of integrins and regulators of actomyosin machinery (ACTN4) and focal adhesion/cytoskeleton dynamics (PXN and VINC). Under mechanical tension, PXN recruits VINC at focal adhesions via a myosin-dependent mechanism, connecting integrins to the actin cytoskeleton and enabling traction and contractility (68). In parallel, ROS-mediated actin oxidation enhances stress fiber formation and actomyosin contractility. Functionally, ATM deletion generates HRD, leading to DNA damage accumulation (6, 8) and increased ROS (55). We propose that mitochondrial reprogramming and elevated ROS in ATM-deficient PDAC enhance contractility and shift the tumor cell secretome toward TGFβ release, driving CAF reprogramming, as supported by ROS interference reducing TGFβ secretion and promoting a more epithelial phenotype. Conversely, pharmacologic ATM inhibition alone elevated ROS and TGFβ1 secretion, indicating that stromal reprogramming arises from the loss of ATM kinase activity rather than HRD-associated genomic alterations. TF analysis identified *Atf6* and *Srebp*, two key regulators of the ER stress response and redox homeostasis, in ATM-deficient malignant cells, suggesting a compensatory response to disrupted redox balance (69).

CAFs promote chemoresistance in PDAC through multiple mechanisms (70). In our models, TGFβ1 KO in ATM-deficient cells reduced migration but did not increase intrinsic sensitivity to FOLFIRINOX, indicating that non-cell-autonomous resistance is driven by TGFβ–dependent myCAF programming. Although stromal barriers can impair drug delivery (67), our *in vivo* data show that TGFβ pathway interference diminishes ECM-producing myCAFs and fibrosis and improves FOLFIRINOX response in ATM-null tumors, independent of P53. Transwell cocultures uncovered an ECM-independent paracrine effect whereby αSMA$^+$ myCAFs enhanced oxaliplatin resistance in ATM-deficient cells, extending prior evidence of CAF-mediated gemcitabine resistance (71) and stromal drug scavenging (72). Early clinical trials combining gemcitabine with TGFβ inhibition showed modest activity in unselected PDAC (52). Consistent with prior reports of no tumor control in KPC upon galunisertib (21), therapeutic benefit was restricted to ATM-depleted PDAC, supporting TGFβ blockade plus chemotherapy in biomarker-defined subsets (ATM loss of function or other HRD genotypes with similar stromal wiring). TGFβ pathway perturbation also affects the immune compartment. Through TGFβ-mediated mechanisms, TAMs and Tregs reinforce PDAC immunosuppression (73), suggesting that anti-TGFβ treatment may induce a more proinflammatory state and synergize with immunotherapy. In ATM-deficient tumors, TGFβ blockade also shifts CAF composition toward iCAF expansion, a reported adaptive reprogramming (21) that may limit response durability by fostering protumorigenic signaling. Nevertheless, the superior efficacy in ATM-deficient PDAC supports integrating context-dependent TME functions into stromal-targeted therapy design.

In conclusion, our study identifies a mechanistic link between ATM deficiency and TGFβ activation in CAFs, driving myCAF reprogramming and PDAC aggressiveness. In this context, therapeutic efficacy relies on dual targeting of intrinsic ATM-deficient cancer cell

(*Continued.*) **H,** ROS levels in *sgKeap1* and *sgCtrl* AKPC and AKC cells. Mean ± SD of 2 cell lines/genotype (tested in ≥3 independent experiments); each dot represents a cell line. **I,** Immunofluorescence for ACTN4 and PXN, and phalloidin-Atto565 staining in *sgKeap1* and *sgCtrl* AKPC and AKC cells with quantification of PXN$^+$, ACTN4$^+$, and F-actin$^+$ staining in DAPI$^+$ cells. Nuclei were counterstained with DAPI. Scale bars, 20 μm. Mean ± SD of five independent experiments (2 cell lines/genotype), each dot represents an experiment. **J,** Incucyte wound-healing assay on *sgKeap1*, *sgActn4*, *sgPxn*, or *sgCtrl* AKC and AKPC cells. Mean ± SD of 2 cell lines/genotype (tested in ≥3 independent experiments); each dot represents a cell line; two-way ANOVA. **K,** ELISA for TGFβ1 in CM from *sgKeap1*, *sgActn4*, *sgPxn*, or *sgCtrl* AKC and AKPC cells. Each dot represents a cell line, with ≥2 CM batches/cell line. **L,** Immunofluorescence for αSMA and SMAD2 p-S465/S467 on PSCs cocultured for 72 hours with *sgKeap1* and *sgCtrl* AKC and AKPC cells and quantification of αSMA$^+$ and SMAD2 p-S465/S467$^+$ PSCs vs. inactivated PSCs. Nuclei were counterstained with DAPI. Scale bars, 20 μm. Mean ± SD of three independent experiments (2 cell lines/genotype), each dot represents an experiment. **A–F, H, I, K,** and **L,** Unpaired Student *t* test. **J,** Two-way ANOVA. *, $P < 0.05$; **, $P < 0.01$; ***, $P < 0.001$; ****, $P < 0.0001$.

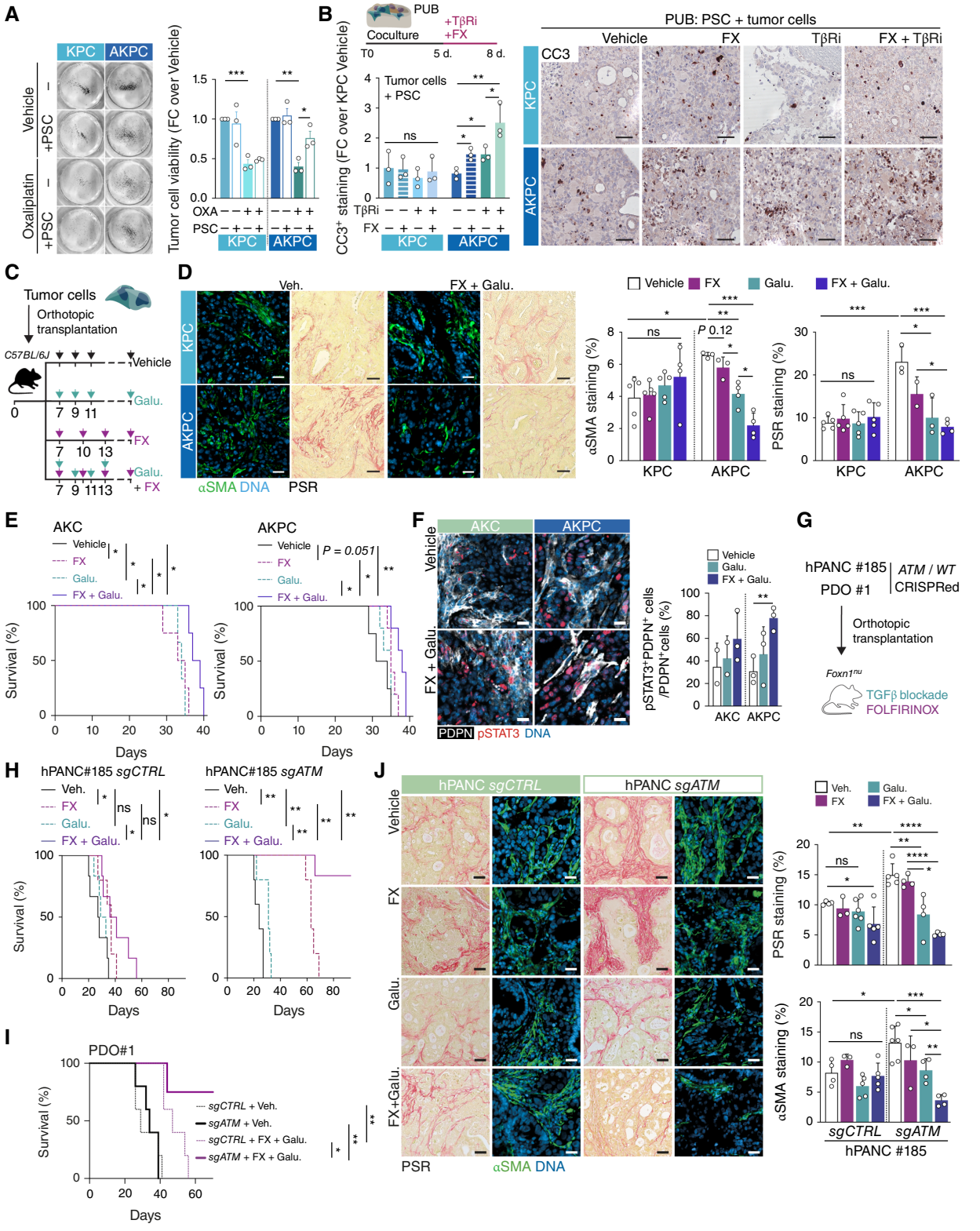


Figure 6.

Perturbing tumor–CAF dialog via TGFβ signaling interference improves FOLFIRINOX efficacy in ATM-deficient PDAC. **A,** Colony formation assay in KPC and KPC tumor cells cocultured or not with PSCs (transwell system) and treated or not with 6 μmol/L oxaliplatin, with quantification of tumor cell viability. Mean ± SD of three independent experiments (≥2 cell lines/genotype), each dot represents an experiment. **B,** Schematic of the (*Continued on the following page.*)

Downloaded from http://aacrjournals.org/cancerres/article-pdf/doi/10.1158/0008-5472.CAN-26-0138/3803456/can-26-0138.pdf by DKFZ - German Cancer Research Center user on 25 June 2026

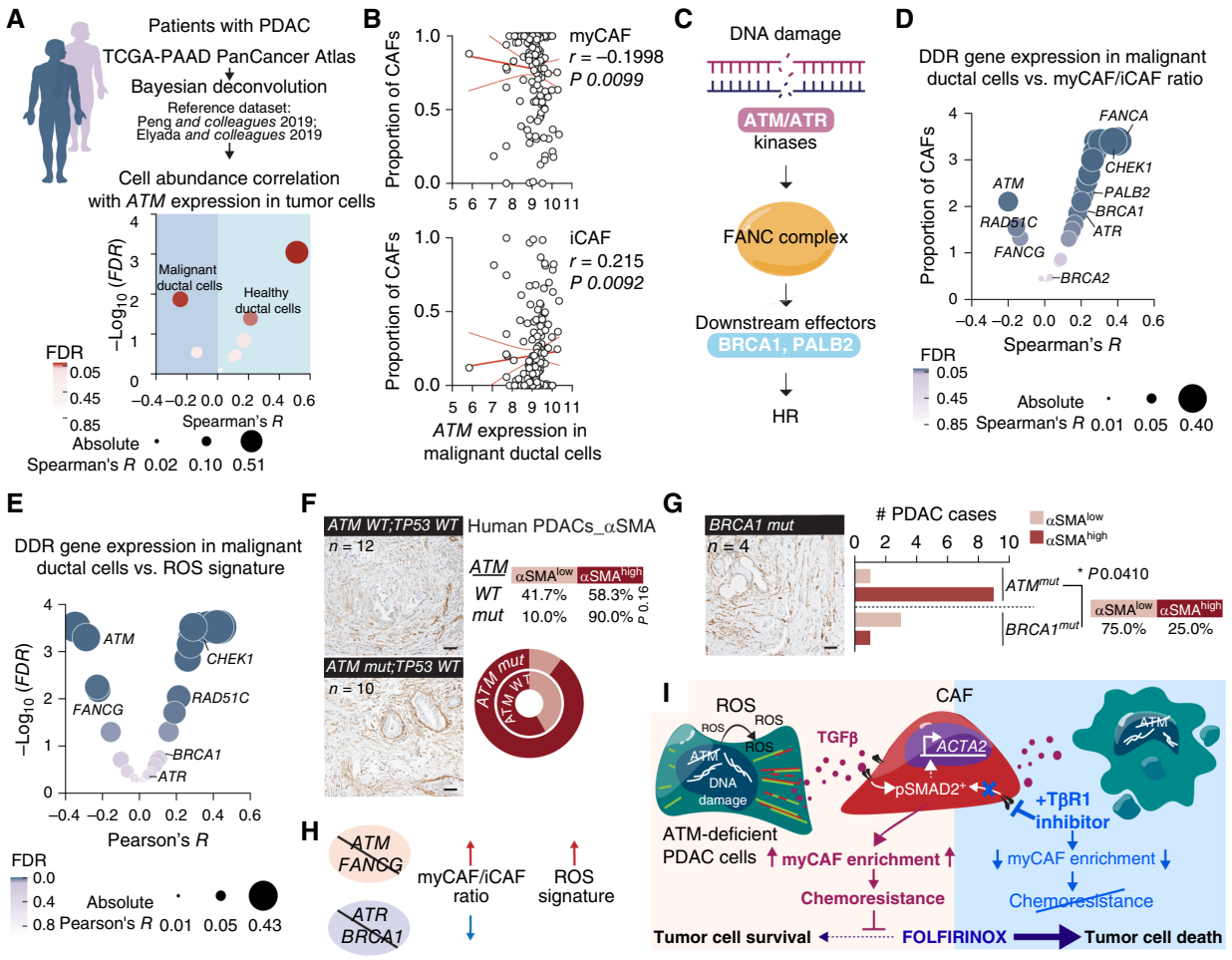


Figure 7.

ATM-deficient human PDACs similarly display a myCAF and ROS-enriched environment. **A,** Workflow for cell type deconvolution and correlation of *ATM* expression with stromal composition using TCGA-PAAD bulk RNA-seq [BayesPrism using two reference datasets (14, 42)], with Spearman correlation between *ATM* expression and cell abundance. **B,** Dot plot showing correlation between *ATM* mRNA expression in malignant ductal cells and inferred myCAF and iCAF proportions. Spearman correlation. **C,** Schematic of DDR signaling and genes investigated in **D–G**. **D** and **E,** Correlation between DDR-related gene expression in inferred malignant ductal cells and myCAF/iCAF ratio (**D**) and ROS signature (**E**). **F,** αSMA IHC in human *TP53* wild-type and *ATM* mutated or not PDACs ($n = 22$) with proportions of low and high αSMA scores. Scale bars, 100 μm. Fisher exact test. **G,** αSMA IHC in human *BRCA1*-mutated PDACs ($n = 4$) with proportions of low and high αSMA scores. Scale bars, 100 μm. Fisher exact test. **H,** Schematic illustrating the correlation between low *ATM*, *ATR*, *BRCA1*, and *FANCG* expression, ROS signature, and CAF differentiation in PDAC. **I,** Model of tumor–CAF interactions in ATM-deficient PDAC and therapeutic implications. *, $P < 0.05$. mut, mutant; WT, wild-type.

vulnerabilities (platin-sensitive) and extrinsic genotype-specific tumor-TME cross-talk (TGFβ-driven), defining a therapeutic strategy for PDAC with ATM loss of function. Although 17% to 25% of PDACs harbor DDR mutations, CAF profiles vary within and across genotypes, requiring validation of genotype-specific stromal patterns before clinical translation. Our work suggests that targeting genotype-specific

(*Continued*.) PUB-based coculture assay, cleaved caspase-3 (CC3) IHC in PSC-tumor cell coculture grafts treated or not with the TGFBR1 inhibitor SB431542 (TβRi; 10 μmol/L) and FOLFIRINOX (FX) and quantification of $CC3^+$ surface. Scale bars, 100 μm. Mean ± SD of three independent experiments (≥2 cell lines/genotype), each dot represents an experiment. **C,** Schematic of the orthotopic assay in **D–F**. **D,** αSMA immunofluorescence and picrosirius red staining in KPC or AKPC orthotopic tumors treated or not with galunisertib (galu.) and FX, with quantification of $αSMA^+$ and picrosirius red-positive surfaces. Nuclei were counterstained with DAPI. Scale bars, 100 μm. Mean ± SD; each dot represents a mouse. **E,** Kaplan–Meier survival of mice orthotopically transplanted with AKC and AKPC tumor cells and treated or not with galu. and FX. **F,** Immunofluorescence for PDPN and STAT3 p-Tyr705 with quantification of $PDPN^+$ $pSTAT3\ p\text{-}Tyr705^+$ cells. Nuclei were counterstained with DAPI. Scale bars, 50 μm. Mean ± SD (≥2 mice/genotype; each dot represents a mouse. **G,** Schematic of the orthotopic assay in **H–J**. **H** and **I,** Kaplan–Meier survival of mice orthotopically transplanted with *sgCTRL* or *sgATM* hPANC#185 (**H**) and *sgCTRL* or *sgATM* PDO#1 (**I**) cells and treated or not with galu. and FX. **J,** Picrosirius red staining and αSMA immunofluorescence in orthotopic tumors, with quantification of $αSMA^+$ and picrosirius red-positive surfaces. Nuclei were counterstained with DAPI. Scale bars, 100 μm. Mean ± SD; each dot represents a mouse. **A, B, D, F,** and **J,** Unpaired Student *t* test. **E** and **H,** Log-rank test. *, $P < 0.05$; **, $P < 0.01$; ***, $P < 0.001$; ****, $P < 0.0001$.

Downloaded from http://aacrjournals.org/cancerres/article-pdf/doi/10.1158/0008-5472.CAN-26-0138/3803456/can-26-0138.pdf by DKFZ - German Cancer Research Center user on 25 June 2026

tumor–stroma interactions can abrogate protumorigenic stromal features and improve treatment response, supporting the integration of mutational and transcriptional profiling with stroma-targeted therapies.

Data Availability

The raw snRNA-seq and ATAC-seq data generated for this project are available on Gene Expression Omnibus with accession number GSE272095. The code used to analyze paired snRNA-seq and ATAC-seq can be found on GitHub at: https://github.com/Gaulton-Lab/atm-deficient-pdac. The bulk RNA-seq data generated for this project are available in the European Nucleotide Archive under accession number PRJEB77788. All LC/MS-MS data files and MaxQuant output files have been deposited in the ProteomeXchange Consortium (http://proteomecentral.proteomexchange.org/PXD042750) via the PRIDE partner repository with the dataset identifier PXD042750. RNA-seq and single-nucleotide variant data from the TCGA-PAAD cohort were obtained from TCGAbiolinks (http://bioconductor.org/packages/TCGAbiolinks/; RRID: SCR_017683; refs. 74, 75). All other raw data generated in this study are available from the corresponding author upon request.

Authors' Disclosures

M.K. Melzer reports grants from Ulm University and EKFS during the conduct of the study. A.-L. Volckmar reports other support from AstraZeneca, Menarini Group, and Novartis outside the submitted work. J. Budczies reports grants from German Cancer Aid and personal fees from MSD outside the submitted work. K.J. Gaulton reports other support from Neurocrine Biosciences, Altos Labs, and Genentech outside the submitted work. K. Steinestel reports personal fees from Bristol Myers Squibb, Merck, Sharp & Dohme, Boehringer Ingelheim, Sanofi, and AstraZeneca outside the submitted work. A. Stenzinger reports other from Agilent Technologies, Aignostics, Amgen, Astellas Pharma, AstraZeneca, Bayer, Bristol Myers Squibb, Eli Lilly and Company, Illumina, Incyte, Janssen Pharmaceuticals, MSD, Novartis, Pfizer, Qlucore, QuiP, Roche, Sanofi, Seagen, Servier, Takeda Pharmaceuticals, and Thermo Fisher Scientific (advisory board/speaker's bureau) and grants from Bayer, Bristol Myers Squibb, Chugai Pharmaceutical, Incyte, and MSD. N. Dusetti reports nonfinancial support from Predicting Med, personal fees from Cure51, and grants and other support from Servier outside the submitted work and a patent for PCT/EP2022/065222 pending and licensed to Predicting Med. L. Perkhofer reports personal fees from AstraZeneca, MSD, Roche, Jazz Pharmaceuticals, and Astellas Pharma outside the submitted work. A. Kleger reports personal fees from Amgen, Sanofi, and Zenas BioPharma outside the submitted work. No disclosures were reported by the other authors.

Authors' Contributions

E. Roger: Conceptualization, formal analysis, supervision, funding acquisition, investigation, visualization, methodology, writing–original draft, project administration. **H.M. Mummey:** Formal analysis, investigation. **E. Zimmer:** Formal analysis, investigation. **D. Srinivasan:** Formal analysis, investigation. **A. Härle:** Formal analysis, investigation. **L. Moubri:** Investigation. **A.K. Michels:** Investigation. **R. Singh:** Investigation. **M. Ekizce:** Formal analysis, investigation. **M.K. Melzer:** Formal analysis, investigation. **Y. Lee:** Formal analysis, investigation. **A. Silva:** Resources, investigation. **L. Härle:** Formal analysis, investigation. **T. Engleitner:** Formal analysis, investigation. **F. Arnold:** Formal analysis, investigation. **M. Morawe:** Resources, formal analysis, investigation. **B.K. Naggay:** Formal analysis, investigation. **J. Schneider:** Formal analysis, investigation. **L. Gilberg:** Investigation. **J.P. Mosler:** Investigation. **C. Ludwig:** Formal analysis, investigation. **C. Meng:** Formal analysis, investigation. **M. Hirschenberger:** Resources. **V. Hunszinger:** Resources. **K. Kluck:** Resources, formal analysis. **M. Kirchner:** Resources, investigation. **A.-L. Volckmar:** Resources, investigation. **M. Wirth:** Resources, formal analysis, investigation. **M.S.S. Alhamdani:** Formal analysis, investigation. **J.D. Hoheisel:** Resources. **J.M. Löhr:** Resources. **T. Seufferlein:** Resources. **A. Abaei:** Resources, formal analysis, investigation. **R. Kemkemer:** Resources. **R. Rad:** Resources, funding acquisition, investigation, project administration. **J. Budczies:** Conceptualization, resources, formal analysis, supervision, funding acquisition, investigation, writing–original draft, project administration. **M.A. Mulaw:** Resources, investigation. **P.C. Hermann:** Resources, investigation. **M.M. Haenle:** Formal analysis. **K.M.J. Sparrer:** Resources. **C.J. Halbrook:** Resources, investigation. **K.J. Gaulton:** Resources. **K. Steinestel:** Formal analysis, investigation. **A. Stenzinger:** Resources. **N. Dusetti:** Resources. **L. Perkhofer:** Resources, formal analysis, funding acquisition, investigation, project administration. **J. Gout:** Conceptualization, resources, formal analysis, supervision, funding acquisition, investigation, methodology, writing–original draft, project administration. **A. Kleger:** Conceptualization, resources, supervision, funding acquisition, writing–original draft, project administration.

Acknowledgments

The authors thank Ariel Asuzano, Jana-Romana Fischer, Randa Kalaajieh, Yvonne Klöpfer, Katrin Köhn, Ralf Köhntop, Claudia Längle, Birgit Ott, Natalie Paul, Julia Ragg, and Sandra Widmann for their outstanding technical support; Ninel Azoitei, Tim Eiseler, and Volker Rasche for scientific discussions; the animal facility Tierforschungszentrum, Ulm University, and its members for animal care; the Organoids core facility (Ulm University) for providing resources and support; and the IPC-CRCM Experimental Pathology Platform for methodology, technical assistance, and anatomic pathology on PDXs. Main funding was provided by Deutsche Krebshilfe 70114761 to A. Kleger. Additional funding to A. Kleger came from Deutsche Forschungsgemeinschaft RTG 3175/1, KL 2544/13-1, KL 2544/10-1, KL 2544/7-1, Heisenberg-Programm KL 2544/6-1, the Deutsche Krebshilfe 70114904, the Hans Beger Stiftung 38080/2.2.3 DMLR, the Baden-Württemberg Stiftung ISF-015, and the BMBF 13N16446. L. Perkhofer was supported by Deutsche Krebshilfe 70115292 and DFG PE 3337/1-1; E. Roger, F. Arnold, and M. Hirschenberger by the Bausteinprogramm of Ulm University (L.SBN.0193, L.SBN.0206, and L.SBN.0245); E. Roger by the Hertha-Nathorff program (Ulm University Hospital); M.K. Melzer by the Clinician Scientist Program (Ulm University) and the Else Kröner Research School for Physicians; and K.M.J. Sparrer by the German Federal Ministry of Research, Technology, and Space (IMMUNOMOD-01KI2014) and the DFG (CRC1279). A. Kleger and T. Seufferlein are speakers of the Else Kröner Research School for Physicians 2023_EKFK.03. A. Kleger and T. Seufferlein were principal investigators, and F. Arnold and D. Srinivasan were students of the HEIST RTG (DFG GRK 2254/1).

Note

Supplementary data for this article are available at Cancer Research Online (http://cancerres.aacrjournals.org/).

Received January 9, 2026; revised April 28, 2026; accepted May 5, 2026; posted first May 8, 2026.

References

1. Siegel RL, Giaquinto AN, Jemal A. Cancer statistics, 2024. CA Cancer J Clin 2024;74:12–49.
2. Halbrook CJ, Lyssiotis CA, Pasca di Magliano M, Maitra A. Pancreatic cancer: advances and challenges. Cell 2023;186:1729–54.
3. Golan T, Hammel P, Reni M, Van Cutsem E, Macarulla T, Hall MJ, et al. Maintenance olaparib for germline BRCA-mutated metastatic pancreatic cancer. N Engl J Med 2019;381:317–27.
4. Javle M, Shacham-Shmueli E, Xiao L, Varadhachary G, Halpern N, Fogelman D, et al. Olaparib monotherapy for previously treated pancreatic cancer with DNA damage repair genetic alterations other than germline BRCA variants: findings from 2 phase 2 nonrandomized clinical trials. JAMA Oncol 2021;7:693–9.
5. Perkhofer L, Gout J, Roger E, Kude de Almeida F, Baptista Simões C, Wiesmüller L, et al. DNA damage repair as a target in pancreatic cancer: State-of-the-art and future perspectives. Gut 2021;70:606–17.
6. Perkhofer L, Schmitt A, Romero Carrasco MC, Ihle M, Hampp S, Ruess DA, et al. ATM deficiency generating genomic instability sensitizes pancreatic ductal adenocarcinoma cells to therapy-induced DNA damage. Cancer Res 2017;77:5576–90.
7. Roger E, Gout J, Arnold F, Beutel AK, Müller M, Abaei A, et al. Maintenance therapy for ATM-deficient pancreatic cancer by multiple DNA damage response interferences after platinum-based chemotherapy. Cells 2020;9:2110.
8. Gout J, Perkhofer L, Morawe M, Arnold F, Ihle M, Biber S, et al. Synergistic targeting and resistance to PARP inhibition in DNA damage repair-deficient pancreatic cancer. Gut 2021;70:743–60.

Downloaded from http://aacrjournals.org/cancerres/article-pdf/doi/10.1158/0008-5472.CAN-26-0138/3803456/can-26-0138.pdf by DKFZ - German Cancer Research Center user on 25 June 2026

9. Moore MJ, Goldstein D, Hamm J, Figer A, Hecht JR, Gallinger S, et al. Erlotinib plus gemcitabine compared with gemcitabine alone in patients with advanced pancreatic cancer: a phase III trial of the National Cancer Institute of Canada Clinical Trials Group. J Clin Oncol 2007;25:1960–6.
10. Connor AA, Gallinger S. Pancreatic cancer evolution and heterogeneity: integrating omics and clinical data. Nat Rev Cancer 2022;22:131–42.
11. Raghavan S, Winter PS, Navia AW, Williams HL, DenAdel A, Lowder KE, et al. Microenvironment drives cell state, plasticity, and drug response in pancreatic cancer. Cell 2021;184:6119–37.e26.
12. Srinivasan D, Gout J, Kleger A, Roger E. Tumor microenvironment subtyping in pancreatic ductal adenocarcinoma: new avenues for personalized therapeutic strategies. Adv Drug Deliv Rev 2025;226:115697.
13. Öhlund D, Handly-Santana A, Biffi G, Elyada E, Almeida AS, Ponz-Sarvise M, et al. Distinct populations of inflammatory fibroblasts and myofibroblasts in pancreatic cancer. J Exp Med 2017;214:579–96.
14. Elyada E, Bolisetty M, Laise P, Flynn WF, Courtois ET, Burkhart RA, et al. Cross-species single-cell analysis of pancreatic ductal adenocarcinoma reveals antigen-presenting cancer-associated fibroblasts. Cancer Discov 2019;9:1102–23.
15. Huang H, Wang Z, Zhang Y, Pradhan RN, Ganguly D, Chandra R, et al. Mesothelial cell-derived antigen-presenting cancer-associated fibroblasts induce expansion of regulatory T cells in pancreatic cancer. Cancer Cell 2022;40:656–73.e7.
16. Rhim AD, Oberstein PE, Thomas DH, Mirek ET, Palermo CF, Sastra SA, et al. Stromal elements act to restrain, rather than support, pancreatic ductal adenocarcinoma. Cancer Cell 2014;25:735–47.
17. Özdemir BC, Pentcheva-Hoang T, Carstens JL, Zheng X, Wu CC, Simpson TR, et al. Depletion of carcinoma-associated fibroblasts and fibrosis induces immunosuppression and accelerates pancreas cancer with reduced survival. Cancer Cell 2014;25:719–34.
18. Olive KP, Jacobetz MA, Davidson CJ, Gopinathan A, McIntyre D, Honess D, et al. Inhibition of hedgehog signaling enhances delivery of chemotherapy in a mouse model of pancreatic cancer. Science 2009;324:1457–61.
19. Mucciolo G, Araos Henríquez J, Jihad M, Pinto Teles S, Manansala JS, Li W, et al. EGFR-Activated myofibroblasts promote metastasis of pancreatic cancer. Cancer Cell 2024;42:101–18.e11.
20. Kim EJ, Sahai V, Abel EV, Griffith KA, Greenson JK, Takebe N, et al. Pilot clinical trial of hedgehog pathway inhibitor GDC-0449 (Vismodegib) in combination with gemcitabine in patients with metastatic pancreatic adenocarcinoma. Clin Cancer Res 2014;20:5937–45.
21. Biffi G, Oni TE, Spielman B, Hao Y, Elyada E, Park Y, et al. IL1-induced JAK/STAT signaling is antagonized by TGFβ to shape CAF heterogeneity in pancreatic ductal adenocarcinoma. Cancer Discov 2019;9:282–301.
22. Waddell N, Pajic M, Patch AM, Chang DK, Kassahn KS, Bailey P, et al. Whole genomes redefine the mutational landscape of pancreatic cancer. Nature 2015;518:495–501.
23. Pishvaian MJ, Bender RJ, Halverson D, Rahib L, Hendifar AE, Mikhail S, et al. Molecular profiling of patients with pancreatic cancer: initial results from the know your tumor initiative. Clin Cancer Res 2018;24:5018–27.
24. Russell R, Perkhofer L, Liebau S, Lin Q, Lechel A, Feld FM, et al. Loss of ATM accelerates pancreatic cancer formation and epithelial-mesenchymal transition. Nat Commun 2015;6:7677.
25. Bernstein JL, Teraoka S, Haile RW, Børresen-Dale AL, Rosenstein BS, Gatti RA, et al. Designing and implementing quality control for multi-center screening of mutations in the ATM gene among women with breast cancer. Hum Mutat 2003;21:542–50.
26. Jackson EL, Willis N, Mercer K, Bronson RT, Crowley D, Montoya R, et al. Analysis of lung tumor initiation and progression using conditional expression of oncogenic K-ras. Genes Dev 2001;15:3243–8.
27. Kawaguchi Y, Cooper B, Gannon M, Ray M, MacDonald RJ, Wright CV. The role of the transcriptional regulator Ptf1a in converting intestinal to pancreatic progenitors. Nat Genet 2002;32:128–34.
28. Marino S, Vooijs M, van Der Gulden H, Jonkers J, Berns A. Induction of medulloblastomas in p53-null mutant mice by somatic inactivation of Rb in the external granular layer cells of the cerebellum. Genes Dev 2000;14:994–1004.
29. Jesnowski R, Fürst D, Ringel J, Chen Y, Schrödel A, Kleeff J, et al. Immortalization of pancreatic stellate cells as an in vitro model of pancreatic fibrosis: deactivation is induced by matrigel and N-acetylcysteine. Lab Invest 2005;85:1276–91.
30. Beutel AK, Schütte L, Scheible J, Roger E, Müller M, Perkhofer L, et al. A prospective feasibility trial to challenge patient-derived pancreatic cancer organoids in predicting treatment response. Cancers (Basel) 2021;13:2539.
31. Dennler S, Itoh S, Vivien D, ten Dijke P, Huet S, Gauthier JM. Direct binding of Smad3 and Smad4 to critical TGF beta-inducible elements in the promoter of human plasminogen activator inhibitor-type 1 gene. EMBO J 1998;17:3091–100.
32. Holle AW, Govindan Kutty Devi N, Clar K, Fan A, Saif T, Kemkemer R, et al. Cancer cells invade confined microchannels via a self-directed mesenchymal-to-amoeboid transition. Nano Lett 2019;19:2280–90.
33. Melzer MK, Breunig M, Lopatta P, Hohwieler M, Merz S, Azoitei A, et al. Protocol to use de-epithelialized porcine urinary bladder as a tissue scaffold for propagation of pancreatic cells. STAR Protoc 2022;3:101869.
34. Hao Y, Hao S, Andersen-Nissen E, Mauck WM 3rd, Zheng S, Butler A, et al. Integrated analysis of multimodal single-cell data. Cell 2021;184:3573–87.e29.
35. Yang D, Moniruzzaman R, Wang H, Wang H, Chen Y. Cross-dataset single-cell analysis identifies temporal alterations in cell populations of primary pancreatic tumor and liver metastasis. Cancers (Basel) 2023;15:2396.
36. Werba G, Weissinger D, Kawaler EA, Zhao E, Kalfakakou D, Dhara S, et al. Single-cell RNA sequencing reveals the effects of chemotherapy on human pancreatic adenocarcinoma and its tumor microenvironment. Nat Commun 2023;14:797.
37. Parekh S, Ziegenhain C, Vieth B, Enard W, Hellmann I. The impact of amplification on differential expression analyses by RNA-seq. Sci Rep 2016;6:25533.
38. Zecha J, Satpathy S, Kanashova T, Avanessian SC, Kane MH, Clauser KR, et al. TMT labeling for the masses: a robust and cost-efficient, in-solution labeling approach. Mol Cell Proteomics 2019;18:1468–78.
39. Marzoq AJ, Mustafa SA, Heidrich L, Hoheisel JD, Alhamdani MSS. Impact of the secretome of activated pancreatic stellate cells on growth and differentiation of pancreatic tumour cells. Sci Rep 2019;9:5303.
40. Alhamdani MS, Youns M, Buchholz M, Gress TM, Beckers MC, Maréchal D, et al. Immunoassay-based proteome profiling of 24 pancreatic cancer cell lines. J Proteomics 2012;75:3747–59.
41. Chu T, Wang Z, Pe'er D, Danko CG. Cell type and gene expression deconvolution with BayesPrism enables Bayesian integrative analysis across bulk and single-cell RNA sequencing in oncology. Nat Cancer 2022;3:505–17.
42. Peng J, Sun BF, Chen CY, Zhou JY, Chen YS, Chen H, et al. Single-cell RNA-seq highlights intra-tumoral heterogeneity and malignant progression in pancreatic ductal adenocarcinoma. Cell Res 2019;29:725–38.
43. Chen K, Wang Q, Li M, Guo H, Liu W, Wang F, et al. Single-cell RNA-seq reveals dynamic change in tumor microenvironment during pancreatic ductal adenocarcinoma malignant progression. EBioMedicine 2021;66:103315.
44. Love MI, Huber W, Anders S. Moderated estimation of fold change and dispersion for RNA-seq data with DESeq2. Genome Biol 2014;15:550.
45. Drifka CR, Loeffler AG, Mathewson K, Keikhosravi A, Eickhoff JC, Liu Y, et al. Highly aligned stromal collagen is a negative prognostic factor following pancreatic ductal adenocarcinoma resection. Oncotarget 2016;7:76197–213.
46. Caronni N, La Terza F, Vittoria FM, Barbiera G, Mezzanzanica L, Cuzzola V, et al. IL-1β^{+} macrophages fuel pathogenic inflammation in pancreatic cancer. Nature 2023;623:415–22.
47. Hosein AN, Huang H, Wang Z, Parmar K, Du W, Huang J, et al. Cellular heterogeneity during mouse pancreatic ductal adenocarcinoma progression at single-cell resolution. JCI Insight 2019;5:e129212.
48. Zhang C, Al-Shaheri FN, Alhamdani MSS, Bauer AS, Hoheisel JD, Schenk M, et al. Blood-based diagnosis and risk stratification of patients with pancreatic intraductal papillary mucinous neoplasm (IPMN). Clin Cancer Res 2023;29:1535–45.
49. Plasari G, Calabrese A, Dusserre Y, Gronostajski RM, McNair A, Michalik L, et al. Nuclear factor I-C links platelet-derived growth factor and transforming growth factor beta1 signaling to skin wound healing progression. Mol Cell Biol 2009;29:6006–17.
50. Batlle E, Massagué J. Transforming growth factor-beta signaling in immunity and cancer. Immunity 2019;50:924–40.
51. Helms EJ, Berry MW, Chaw RC, DuFort CC, Sun D, Onate MK, et al. Mesenchymal lineage heterogeneity underlies nonredundant functions of pancreatic cancer-associated fibroblasts. Cancer Discov 2022;12:484–501.
52. Melisi D, Garcia-Carbonero R, Macarulla T, Pezet D, Deplanque G, Fuchs M, et al. Galunisertib plus gemcitabine vs. gemcitabine for first-line treatment of patients with unresectable pancreatic cancer. Br J Cancer 2018;119:1208–14.
53. Kemp SB, Cheng N, Markosyan N, Sor R, Kim IK, Hallin J, et al. Efficacy of a small-molecule inhibitor of KrasG12D in immunocompetent models of pancreatic cancer. Cancer Discov 2023;13:298–311.

Downloaded from http://aacrjournals.org/cancerres/article-pdf/doi/10.1158/0008-5472.CAN-26-0138/3803456/can-26-0138.pdf by DKFZ - German Cancer Research Center user on 25 June 2026

54. Hinz B. The extracellular matrix and transforming growth factor-β1: tale of a strained relationship. Matrix Biol 2015;47:54–65.
55. Srinivas US, Tan BWQ, Vellayappan BA, Jeyasekharan AD. ROS and the DNA damage response in cancer. Redox Biol 2019;25:101084.
56. Jiang J, Wang K, Chen Y, Chen H, Nice EC, Huang C. Redox regulation in tumor cell epithelial-mesenchymal transition: molecular basis and therapeutic strategy. Signal Transduct Target Ther 2017;2:17036.
57. Pillai R, Hayashi M, Zavitsanou AM, Papagiannakopoulos T. NRF2: KEAPing tumors protected. Cancer Discov 2022;12:625–43.
58. Legerstee K, Houtsmuller AB. A layered view on focal adhesions. Biology (Basel) 2021;10:1189.
59. Singh RR, O'Reilly EM. New treatment strategies for metastatic pancreatic ductal adenocarcinoma. Drugs 2020;80:647–69.
60. De Jesus-Acosta A, Sugar EA, O'Dwyer PJ, Ramanathan RK, Von Hoff DD, Rasheed Z, et al. Phase 2 study of vismodegib, a hedgehog inhibitor, combined with gemcitabine and nab-paclitaxel in patients with untreated metastatic pancreatic adenocarcinoma. Br J Cancer 2020;122:498–505.
61. Cancer Genome Atlas Research Network. Integrated genomic characterization of pancreatic ductal adenocarcinoma. Cancer Cell 2017;32:185–203.e13.
62. Shaashua L, Ben-Shmuel A, Pevsner-Fischer M, Friedman G, Levi-Galibov O, Nandakumar S, et al. BRCA mutational status shapes the stromal microenvironment of pancreatic cancer linking clusterin expression in cancer associated fibroblasts with HSF1 signaling. Nat Commun 2022;13:6513.
63. Lavin MF, Scott S, Gueven N, Kozlov S, Peng C, Chen P. Functional consequences of sequence alterations in the ATM gene. DNA Repair (Amst) 2004;3:1197–205.
64. Ho WJ, Jaffee EM, Zheng L. The tumour microenvironment in pancreatic cancer - clinical challenges and opportunities. Nat Rev Clin Oncol 2020;17:527–40.
65. Camp D, Venkatesh B, Solianova V, Varela L, Goult BT, Tanentzapf G. The actin binding sites of talin have both distinct and complementary roles in cell-ECM adhesion. PLoS Genet 2024;20:e1011224.
66. Cheung EC, DeNicola GM, Nixon C, Blyth K, Labuschagne CF, Tuveson DA, et al. Dynamic ROS control by TIGAR regulates the initiation and progression of pancreatic cancer. Cancer Cell 2020;37:168–82.e4.
67. Vennin C, Mélénec P, Rouet R, Nobis M, Cazet AS, Murphy KJ, et al. CAF hierarchy driven by pancreatic cancer cell p53-status creates a pro-metastatic and chemoresistant environment via perlecan. Nat Commun 2019;10:3637.
68. Bays JL, DeMali KA. Vinculin in cell-cell and cell-matrix adhesions. Cell Mol Life Sci 2017;74:2999–3009.
69. Zhang Z, Zhang L, Zhou L, Lei Y, Zhang Y, Huang C. Redox signaling and unfolded protein response coordinate cell fate decisions under ER stress. Redox Biol 2019;25:101047.
70. Beatty GL, Werba G, Lyssiotis CA, Simeone DM. The biological underpinnings of therapeutic resistance in pancreatic cancer. Genes Dev 2021;35:940–62.
71. Dalin S, Sullivan MR, Lau AN, Grauman-Boss B, Mueller HS, Kreidl E, et al. Deoxycytidine release from pancreatic stellate cells promotes gemcitabine resistance. Cancer Res 2019;79:5723–33.
72. Hessmann E, Patzak MS, Klein L, Chen N, Kari V, Ramu I, et al. Fibroblast drug scavenging increases intratumoural gemcitabine accumulation in murine pancreas cancer. Gut 2018;67:497–507.
73. Principe DR, Timbers KE, Atia LG, Koch RM, Rana A. TGFbeta signaling in the pancreatic tumor microenvironment. Cancers (Basel) 2021;13:5086.
74. Colaprico A, Silva TC, Olsen C, Garofano L, Cava C, Garolini D, et al. TCGAbiolinks: an R/Bioconductor package for integrative analysis of TCGA data. Nucleic Acids Res 2016;44:e71.
75. Mounir M, Lucchetta M, Silva TC, Olsen C, Bontempi G, Chen X, et al. New functionalities in the TCGAbiolinks package for the study and integration of cancer data from GDC and GTEx. PLoS Comput Biol 2019;15:e1006701.

Downloaded from http://aacrjournals.org/cancerres/article-pdf/doi/10.1158/0008-5472.CAN-26-0138/3803456/can-26-0138.pdf by DKFZ - German Cancer Research Center user on 25 June 2026